Colliding Galaxies in a (Nut)Shell

Jonathan Petersson

Lund Observatory
Lund University

2022-EXA194

Degree project of 60 higher education
credits (for a degree of Master)

May 2022

Supervisor: Florent Renaud

Lund Observatory
Box 43
SE-221 00 Lund
Sweden

Abstract

Galaxy interactions and mergers are natural recurring events in the current cosmological paradigm, events that often coincide with starbursts and enhanced star formation activity. To understand why that is, one can use idealised (non-cosmological) merger simulations, which provide freedom to recreate specific tidally distorted galaxies, and analysis of the time evolution and underlying physics of the star formation activity at a high spatial resolution.

One particular class of tidally distorted galaxies are shell galaxies. These galaxies are characterised by wide concentric shell(s), that extends out to large galactocentric distances with sharp outer edges. Shells, together with other unique morphological tidal features, have shown to be remnants of previous merger events, and can therefore serve as a powerful tool to help reconstruct assembly histories of galaxies. An example of where this have been put in action, is the shell galaxy NGC 474 and its outer shell. However, besides constraints on its formation history, observations have also found evidence of young massive star clusters in its outer shell, which asks questions about where and when star formation takes place in shell-forming mergers and shell galaxies.

The purpose of this project is to study the merger-driven star formation activity in a shell galaxy, how it evolves with time and within the system, and the physical conditions for it. To fulfil this, we perform idealised merger simulations. We begin with a short parameter survey, in which we explore different sets of initial conditions, to find the most favourable orbital configuration for shell formation. The conclusion is a near-radial intermediate to major merger (1:10 to 1:2 mass ratio) between two disk galaxies. From this, we perform an idealised high-resolution *N*-body + hydrodynamical simulation of two merging galaxies and their formation into a shell galaxy, and analyse its star formation activity.

In our analysis, we find that as the system approaches the first pericentre passage, it goes into a starburst phase with enhanced star formation activity, due to an excess of dense gas generated. For spatially resolved star formation, the Kennicutt-Schmidt relation varies during the merger, but with no general trend over time. A break is consistently shown in the relation at low gas surface densities, due to mixing of atomic HI and molecular H_2 gas. By analysing HI and H_2 individually, we find that the surface density of H_2 shows a better correlation to the surface density of SFR than that for all the gas, while for HI, we see the opposite with no correlation at all. Star formation therefore mainly takes place in regions with large amounts of H_2 gas, including the nucleus, spiral arms, and occasionally in the outskirts of the system early in the merger.

Tidal interactions during the merger scatters stars into a stellar spheroid around the system, and as the system approaches coalescence, morphological quenching stops star formation (without the need of AGN feedback). Only the innermost ~1.5 kpc is left with star-forming H_2 gas. The first stellar shell does not appear until after coalescence, and due to its position at a large galactocentric distance and lack of gas, it shows an absence of in situ star formation, and so does forthcoming stellar shells as well. Our results suggest that shell-forming mergers can be part of the process in turning blue-late types galaxies into red and dead early-types ones in

galaxy evolution, including blue nuggets into red ones at high redshift, due to similarities with the compaction model. However, further investigation of this calls for more simulations, both idealised and cosmological, which would provide valuable statistics on e.g what the effects the orbital properties, mass ratio and continues accretion of gas would have on the quenching phase.

Popular Science Summary

How galaxies interact with each other, and what effect(s) this has on star formation, is a key ingredient for understanding how galaxies form and evolve. Interactions between galaxies can often times lead to so-called merger events, where two galaxies collide and merge into one. In these merger events, unique morphological tidal features can be produced, and be left behind to remain visible long after the merger event itself. Tidal features are therefore a powerful tool to help reconstruct assembly histories of galaxies. An example of where this has been put in action, is the galaxy NGC 474 and its outer shell, which is a tidal feature that can be described as a wide concentric arc of stars. Besides constraints on its formation history, observations have also shown that NGC 474's outer shell contains several massive star clusters, two of which that are much younger than the overall population of stars in the shell itself. Instead, they match a population of stars close to the nucleus of NGC 474. This shows evidence of a rather complex star formation history, and raises questions about where star formation takes place, the conditions for it, and how it evolves in these types of mergers and galaxies with shells: shell galaxies.

In this project, we perform two sets of numerical simulations. The first involves a parameter survey, where we explore different sets of parameters between two colliding galaxies, to see what configuration is the most favourable for shell formation. In order to get a shell galaxy with distinct shells, the results suggest a merger between two disk galaxies on a head-on trajectory towards each other, with a mass ratio between 1:10 to 1:2. With this information, we perform our second set of simulations, which is a single high-resolution simulation of a merger and its formation into a shell galaxy.

The results from our high-resolution simulation show evidence of three epochs of star formation. Pericentre passages are when the two galaxies are as closest to each other. Before the first pericentre passage, the rate at which stars form is relatively stable, however, as the two galaxies approach the first passage, the star formation activity increases. This is due to interactions between the galaxies' gas reservoirs, which generates an excess of dense gas that can form stars. During the merger event, gravitational interactions puffs up the disk of stars, such that the gravitational force on the gas becomes weaker. Because of this, the gas can not get dense enough to form stars, which causes the star formation activity to go into its third and last epoch, where the rate at which stars form is close to zero.

On a local scale, our high-resolution simulation shows indications of different behaviours between regions with high and low fraction of molecular H_2 gas. Regions with a high fraction of H_2 correlates better to a classical star formation law, where the rate at which stars form is proportional to the gas density, than regions with a low fraction of H_2. The central areas of the two galaxies, and later the shell galaxy, show evidence of large fractions of H_2. This is also where many of the star-forming regions are located, however, we also see star formation in spiral arms and in the outskirts early in the merger. As the two galaxies evolve into a shell galaxy, only the innermost area close to the nucleus of the galaxy contains star-forming molecular H_2 gas. Since shells form at large distances from the nucleus, and contain very little star-forming

gas, our simulation suggests that there is no star formation in shells.

In conclusion, assuming that our high-resolution simulation forms a ‘typical’ shell galaxy, and therefore is representative for shell galaxies as a whole, our results suggest that the two young massive star clusters in NGC 474’s outer shell, have an external origin. Our simulation instead advocates for a formation scenario where the star clusters were formed during a merger event with enhanced star formation activity, when the material that later formed the shell was close to the associated material of the nucleus.

Acknowledgements

At first, I would like to thank my supervisor Florent Renaud, for his incredible support and valuable guidance throughout this project. Without it, none of this would have been possible. I would also like to thank my friends and family for always being there and supporting me.

Contents

1 Introduction **3**
1.1 Shell galaxies 4

2 Parameter Survey **7**
2.1 Mass ratio 8
2.2 Pericentre distance 9
2.3 Inclination angle 9
2.4 Morphology 10
2.5 Summary 10

3 High-resolution simulation **11**

4 Conclusions **23**

A Additional plots **27**

Chapter 1

Introduction

In the standard cosmological model (ΛCDM), galaxies form and build up their stellar mass via continuous processes of accretion of gas, and successive mergers with other galaxies (White & Rees, 1978). As two galaxies merge, so-called low surface brightness objects (LSB) can often times be produced, and can be described as unique morphological tidal features, such as stellar streams, tidal tails, plumes and shells, that have been left behind in the galaxies' stellar haloes long after the merger event itself (Mihos et al., 2005; Martínez-Delgado et al., 2010; Duc et al., 2015; Mancillas et al., 2019a). In this project, our focus is on one particular type of tidal feature: shells, which can be described as a wide concentric stellar arcs, extending out to large galactocentric distances, with sharp outer edges.

Since shells (together with other tidal features) are a product of merger events, they can serve as a powerful tool to help reconstruct assembly histories of galaxies (Arnaboldi et al., 2012; Romanowsky et al., 2012; Foster et al., 2014; Longobardi et al., 2015; Amorisco, 2015). By knowing the formation mechanisms and morphology of tidal features, we can use them to constrain the orbital properties and mass ratios of satellite galaxies at accretion with a larger galaxy (Johnston et al., 2008; Hendel & Johnston, 2015). Specific for shells, the number and distribution of them can help constrain the mass distribution of their host galaxy, as well as the time of the merger event itself (Quinn, 1984; Dupraz & Combes, 1986; Canalizo et al., 2007). Tidal features are also useful for measurements of the gravitational potential in low-acceleration regimes of galaxies (Merrifield & Kuijken, 1998; Ebrová et al., 2012).

So, by studying shells and other tidal features, we can constrain the merger history of galaxies, and from that expand our knowledge about the role of mergers in galaxy formation and evolution. We can also potentially learn more about our own Galaxy. There have been indications that the Milky Way itself might posses multiple shells around it (Deason et al., 2013; Donlon et al., 2020), shells that can be a new source of information regarding the formation history of the Milky Way.

However, throughout the last few decades, research regarding shells has mostly been focused on their formation mechanisms (e.g. Quinn, 1984; Hernquist & Spergel, 1992; Amorisco, 2015; Hendel & Johnston, 2015; Pop et al., 2018; Karademir et al., 2019). The detection of young massive star clusters in the prominent outer shell of NGC 474 (Fensch et al., 2020) (for more details, see the introduction section in Chap. 3), highlights the need for a dedicated study of the star formation activity in shell-forming mergers and the galaxies they produce: shell galaxies.

The purpose of this project is to study the star formation activity in two merging galaxies and their formation into a shell galaxy. Examples of questions that we want to address are as follows. How does the star formation activity evolve with time and within the system? What are the physical conditions for star formation? Do shells host in situ star formation? If not, why?

To answer these questions, we first need to find an set of initial conditions favourable for shell formation. This is done via a short parameter survey in Chap. 2, where we explore different sets of parameters and study their influence on shell formation. With an orbital configuration favourable for shell formation, we perform an idealised high-resolution merger simulation, and analyse its star formation activity. We present this in Chap. 3, in the form of a self-contained paper. In Chap. 4, we give a project-oriented conclusion, and for the rest of Chap. 1, we give a short background about observations of shell galaxies and formation mechanisms of shells.

1.1 Shell galaxies

In comparison to gas rich tidal tails (Duc et al., 2011), shells are relatively gas poor[1] (Fort et al., 1986; Weil & Hernquist, 1993; Mancillas et al., 2019b). Shells' relatively faint stellar components are therefore usually only available for spectroscopic analysis, making them difficult to detect. However, despite the challenges with detecting shells, the first tidally distorted galaxies with stellar shells around them, i.e. shell galaxies, were already reported in in the Atlas of Peculiar Galaxies in 1966 (Arp, 1966). With the introduction of post-processing to help reveal shell structures, Malin & Carter (1983) were able to identity 137 shell galaxies, and since then, several hundreds of shell galaxies have been identified (e.g. Thronson et al., 1989; Tal et al., 2009; Atkinson et al., 2013; Duc et al., 2015; Bílek et al., 2020). Three examples of shell galaxies can be seen in Fig. 1.1. NGC 474 (left panel) contains some of the most brightest known stellar shells at around 25 mag arcsec^{-2} in the R-band (Turnbull et al., 1999). Observations have shown that shells are more frequent around early type galaxies than in blue type ones (Atkinson et al., 2013), and it has been estimated that around ~20% of elliptical and lenticular galaxies exhibit one or more shells (Malin & Carter, 1983; Tal et al., 2009; Duc et al., 2015; Pop et al., 2018; Bílek et al., 2020).

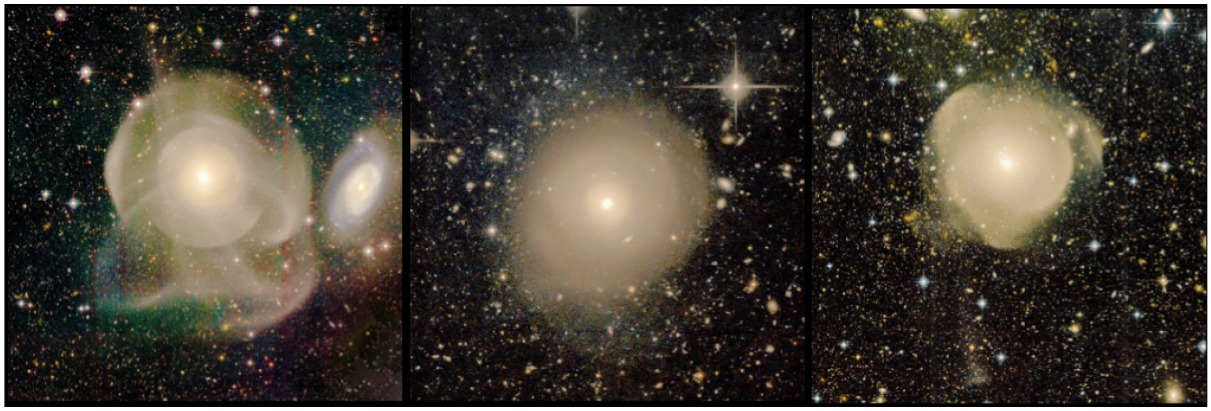

Figure 1.1: True colour images (using g, r and i bands) of three shell galaxies from the ATLAS^{3D} project, obtained with the MegaCam camera at the Canada–France–Hawaii Telescope (Duc et al., 2015). From left to right, NGC 474, NGC 502 and NGC 3619.

As mentioned earlier, shells and shell galaxies are a product of merger events. The most widely accepted formation scenario of shells is the phase-space wrapping model, originally suggested by Quinn (1984). Without going into much detail, the scenario suggests that shells form via intermediate to major mergers (i.e. a mass ratio $\gtrsim$1:10) (Pop et al., 2018), with satellite galaxies on near-radial orbits. Less eccentric orbits tend to produce more tidal tails and stellar

[1]However, see Charmandaris et al. (2000).

streams (Amorisco, 2015; Hendel & Johnston, 2015). During these mergers, stars are tidally stripped from the satellite, and begin to oscillate in the gravitational potential of the system with different orbital periods. With time, tidally stripped stars will start to wrap in phase-space and accumulate at the apocentres of their orbits, forming shells with sharp outer edges, extending out to large galactocentric distances. A sketch showing the formation processes of stellar shells can be seen in Fig. 1.2. In Fig. 1.3, we show an example of a shell galaxy from one of our simulations, and that stars from a tidally stripped satellite forms a distinct shell structure around the galaxy. In Fig. 1.4, we illustrate the wrap in phase-space of the shell galaxy in Fig. 1.3.

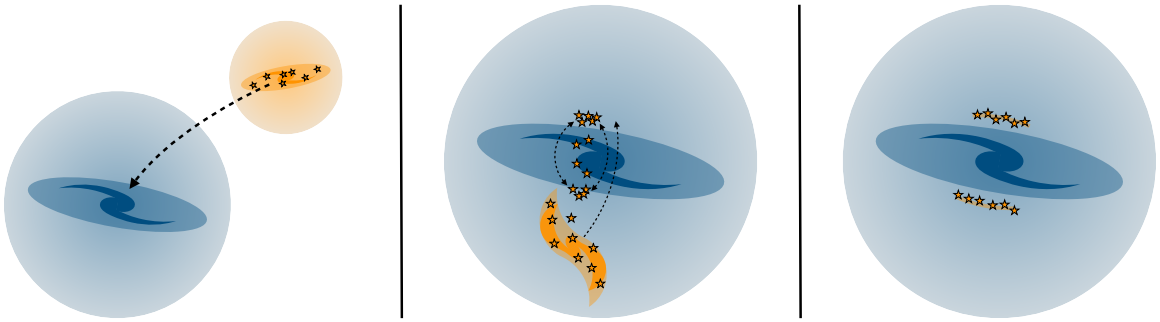

Figure 1.2: Sketch showing the formation of stellar shells. A less massive satellite galaxy (coloured orange) merges with a more massive main galaxy (coloured blue) on a near-radial orbit. Tidally stripped stars from the satellite starts to oscillate in the gravitational potential of the system, and begins to accumulate at the apocentres of their orbits to form sharp stellar shells at large galacocentric distances.

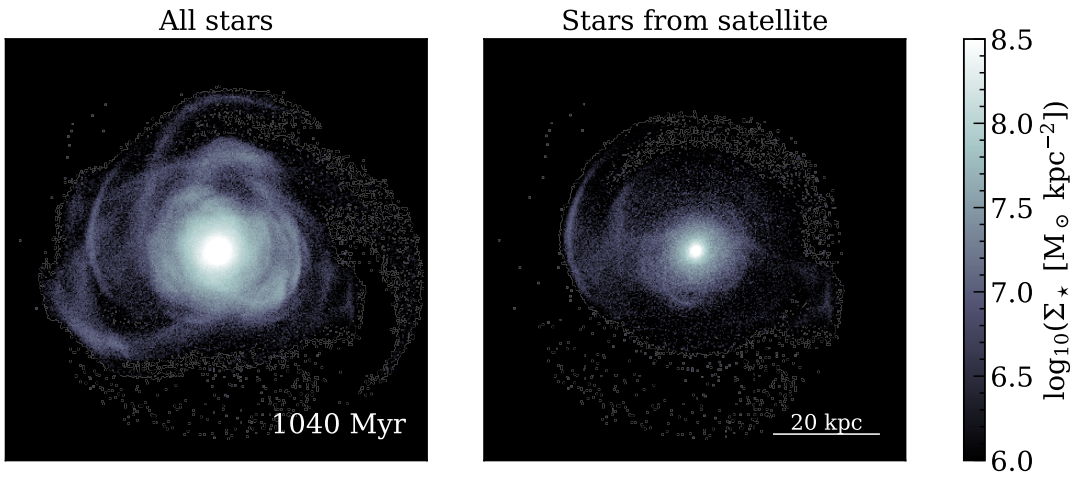

Figure 1.3: Stellar surface density maps of a shell galaxies from one of our merger simulations (1040 Myr after the first pericentre passage). By only looking at stars from the tidally disrupted satellite, a distinct shell structure, extending out to large galactocentric distances can be seen.

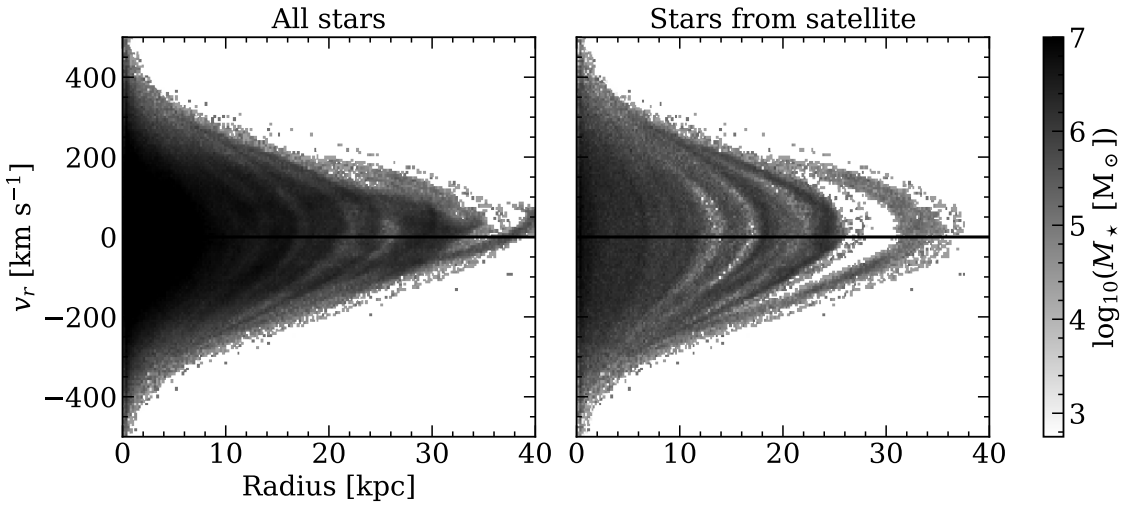

Figure 1.4: Stellar mass-weighted phase-space (v_r versus r) distributions for the stellar surface density maps in Fig. 1.3. The stellar shells from the disrupted satellite corresponds to wraps in phase-space, in agreement with the phase-space wrapping model by Quinn (1984).

Chapter 2

Parameter Survey

Our parameter survey begins with a so-called fiducial run, with initial conditions chosen to be in line with what previous research tells us is the most favourable for shell formation, i.e. a near-radial intermediate to major ($\gtrsim$1:10 mass ratio) merger (Quinn, 1984; Hernquist & Spergel, 1992; Karademir et al., 2019; Pop et al., 2018). We perform our fiducial run using the Adaptive Mesh Refinement (AMR) code RAMSES (Teyssier, 2002), with a maximum physical resolution of ~49 pc. The simulation includes a main galaxy, initially placed at $(x, y, z) = (0, 0, 0)$ with zero net velocity, and a satellite a few tens of kpc away, with a trajectory towards the main one. The full orbital properties of the satellite are given in Table 2.1. Both galaxies are modelled using the MAGI code (Miki & Umemura, 2018), with a dark matter halo, central bulge, and in the case of a disk galaxy, a stellar and a gaseous disk. The simulation is fully N-body + hydrodynamical, however, to save computational power and time, we do not allow any star formation to occur (by making the gas isothermal).

The method we use to detect shells, consists of analysing stellar surface density profiles, one for each galaxy and one with both galaxies included, together with a visual inspection of the stellar surface density map of the system. We illustrate this method for our fiducial run in Fig. 2.1. In the top left panel, we plot the stellar surface density versus radius at ~367 Myr after the first pericentre passage. Stellar shells are described as wide concentric arcs, extending out to large galactocentric distances with sharp outer edges, i.e. overdensities with sharp cut offs at large radii in the stellar surface density profile is an indication of a potential shell. We look for these overdensities via exponential fits of the stellar surface density profiles (disk galaxies typically have a close to exponential surface brightness/density profile Freeman, 1970)). It is within the grey area ($2 < r$ [kpc] < 10) that we do our exponential fits. The stellar surface density profiles deviate too strongly from an exponential fit outside this range. This is due the presence of a bulge at small radii, and tidal features from the merger at larger radii. We then subtract each stellar surface density profile with its respective exponential fit, and plot the residuals as a function of radius (bottom left panel). Overdensities with respect to an exponential profile corresponds to a high sharp peak in the residuals plot, and is an indication of a potential shell. For our fiducial run in Fig. 2.1, we can see an example of such a peak at $r = 20$ kpc. However, this is not sufficient evidence of a stellar shell, since other tidal features at large radii also can produce a similar signal. To complement our analysis, we do a visual inspection of the stellar surface density map of the system, to see if we can visually identify a shell at this radius. In Fig. 2.1 (right), we show the visual inspection for the peak at $r = 20$ kpc in our fiducial run, and find that it corresponds to an 'umbrella'-like shell in the top right part of the galaxy.

With this detection method, we now present our parameter survey. The survey includes 10 low-resolution simulations (with similar numerical set-ups as in the fiducial run), in which we

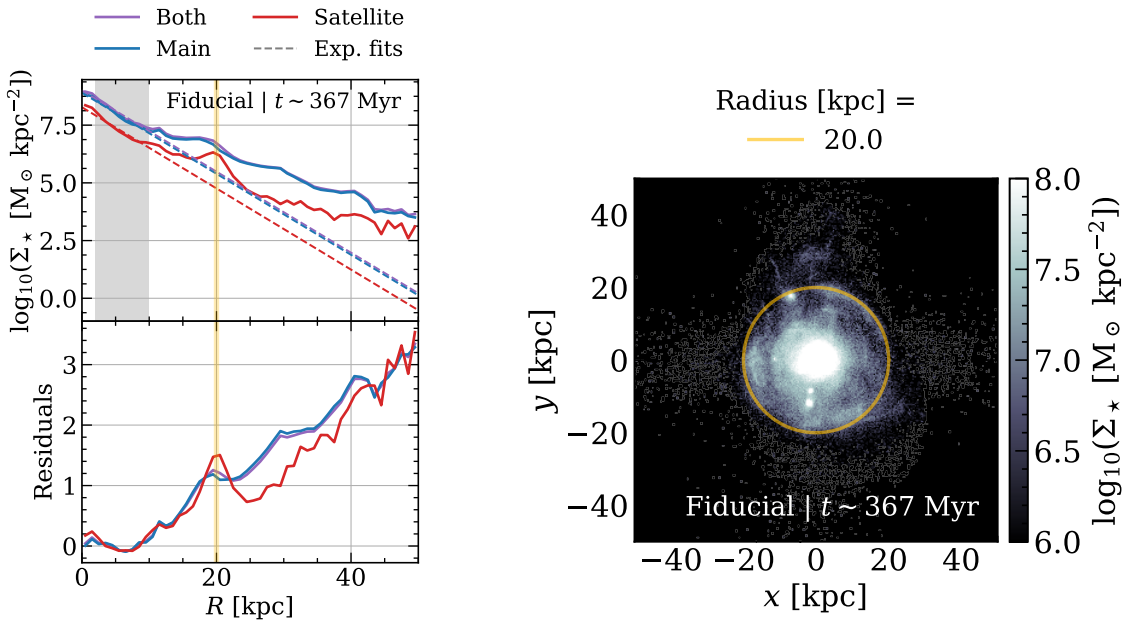

Figure 2.1: *Top left:* Stellar surface density profiles for our fiducial run at ~367 Myr after the first pericentre passage, one for each galaxy and one with both galaxies included. Dashed lines are exponential fits, derived from the data within the grey area ($2 < r$ [kpc] < 10). *Bottom left:* Residuals plot showing how much each stellar surface density profile deviates from their respective exponential fit. *Right:* Stellar surface density map of all stars, t ~367 Myr after the first pericentre passage. The yellow circle corresponds to the yellow vertical line in the residuals plot, and shows that the peak coincide with a 'umbrella'-like shell in the top right part of the galaxy.

explore different sets of parameters and investigate their influence on shell formation. However, instead of analysing each individual simulation step by step, we summarise our findings with respect to the parameters that we explore. This includes mass ratio, morphology of the satellite, and orbital properties such as pericentre distance and inclination angle (with respect to the plane of the main galaxy). For details on what parameters we use for the satellite in each of our 10 simulations, see Table 2.1. For results similar to what we present in Fig. 2.1, but for our suite of simulations in Table 2.1, see Fig. A.1–A.5. Time indications in Fig. A.1–A.5 are all with respect to the first pericentre passage in each respective simulation. These time indications are however only rough estimates, since the time of the first pericentre passage of each simulation are all obtained visually from movies due to storage limitations in number of outputs with raw data.

2.1 Mass ratio

We perform three simulations with mass ratios 1:5, 1:10 and 1:20 (M1, M2 and M3 respectively in Fig. A.1, A.2 and A.4). All other parameters remain the same as in the fiducial run. We find that by decreasing the mass ratio, shell formation do not stop, but instead gets weaker with fainter shells. Since the fraction of stars from the satellite is lower when the mass ratio decreases, shells will naturally have a lower surface mass density, making them more difficult to detect. Due to their low surface mass density, there is also a higher risk that shells from

Table 2.1: Sets of orbital configurations for the satellite in each simulation in our parameter survey.

Simulation	Mass ratio	(x, y, z) [kpc]	(v_x, v_y, v_z) [km s^{-1}]	Inc. [deg]	Morph.
Fiducial	1:2	(60, 10, 0)	(−30, 0, 0)	0	Disk
M1	1:5	—"—	—"—	—"—	—"—
M2	1:10	—"—	—"—	—"—	—"—
M3	1:20	—"—	—"—	—"—	—"—
P1	1:2	(60, 30, 0)	(−30, 30, 0)	—"—	—"—
P2	—"—	—"—	(−30, 60, 0)	—"—	—"—
P3	—"—	—"—	(−30, 120, 0)	—"—	—"—
I1	—"—	(60, 0, 0)	(−30, 0, 0)	45	—"—
I2	—"—	—"—	—"—	90	—"—
I3	—"—	—"—	—"—	180	—"—
T1	—"—	(60, 10, 0)	—"—	0	Elliptical

the tidally disrupted satellite gets 'hidden' behind other tidal structures. All this agrees well with Pop et al. (2018), who study the incidence and formation processes of shell galaxies in the cosmological gravity+hydrodynamics Illustris simulation, and find that shell galaxies form preferentially through relatively major mergers ($\gtrsim$ 1:10 stellar mass ratio).

2.2 Pericentre distance

In our parameter survey, we run three simulations with increasing pericentre distances (P1, P2 and P3 in Fig. A.2 and A.4). We increase the pericentre distance by giving the satellite a higher initial position in y, and by adding a initial velocity in the y-direction. The results suggest that when the pericentre distance increases, the merger is more likely to produce stellar streams and tidal tails instead of shells. There are still shells, but weaker and more difficult to detect due to overlaps with other tidal features. Once again, our results agrees with previous research, i.e. that satellites on less eccentric orbits tend tend to produce more stellar streams and tidal tails instead of shells (Amorisco, 2015; Hendel & Johnston, 2015)

2.3 Inclination angle

In our suite of simulations, we explore the influence of the inclination angle of the satellite with respect to the plane of the main galaxy, for three different angles: 45, 90 and 180 deg (I1, I2, and I3 respectively) (Fig. A.3 and A.5). Worth highlighting is that instead of changing the position of the satellite, we change the direction of the spin axis of the main galaxy to obtain an inclination angle. For the 45 and 90 deg simulations, the results show that besides the different viewing angles (due to the change in direction of the spin vector) the inclination angle do not seem to have substantial impact on shell formation.

One would expect that the difference in dynamical friction between a satellite travelling on a trajectory with 0 deg inclination angle (practically through the disk of the main galaxy), to the case with a 90 deg inclination angle, would result in a difference in how far away shells can form. A 90 deg inclination angle would result in shells at larger galactocentric distances and vice versa for a 0 deg inclination angle. However, from this relatively short parameter survey, we can not draw any conclusions from this.

The simulation with an 180 deg inclination angle is a special case, because we practically flip the galaxy and change the main galaxy's rotation to the opposite direction, i.e. the orbit of the satellite is now retrograde. In general, this leads to a weaker gravitational pull, due to a higher relative velocity between stars in the two galaxies. However, in this specific simulation, where we have a near-radial orbit, this effect is less important. The result is therefore similar to the simulations with a 45 and 90 deg inclination angle, i.e. the inclination angle does not seem to have an important impact on shell formation. This is also one of the conclusion in Karademir et al. (2019), that for short pericentre distances, shell structures are independent of the inclination angle.

2.4 Morphology

The final parameter (or property) that we explore in our parameter survey is the the morphology of the satellite. We only perform one simulation of this (T1, Fig. A.3 and A.5), in which we change the satellite from a disk to an elliptical galaxy. One major difference between these two morphologies, is that stars are more 'grouped up' in phase space in a disk galaxy with rotation, organisation and structures (e.g. spiral arms), compared to in an elliptical galaxy, where stars are more spread out in phase space with more random motions and less structures. This difference can be seen in our simulation, where we still get shells, but they are wider and more spread out radially, which makes them fainter and therefore more difficult to detect. Our results once again correlates well with Pop et al. (2018), who find that shell forming progenitors typically have a high mean $\kappa_{\rm rot}$, which is the fraction of kinetic energy invested in ordered rotation. This means that shell forming progenitors are more rotation dominated, and therefore more likely disk galaxies.

2.5 Summary

To summarise, stellar shells seems to form in a large variety of mergers. All parameters (that we explore), except the inclination angle, have an influence on shell formation, typically in the form of shells' stellar surface density, or how easily distinguishable shells are in comparison to other tidal features. However, none of the orbital configurations that we explore in our parameter survey, give more distinct stellar shells than what we already get in our fiducial run. We therefore conclude that from our parameter survey, the most favourable orbital configuration for stellar shells, is a near-radial merger between two disk galaxies, with a mass ratio of ~1:2, and with no dependence on the inclination angle with respect to the plane of main galaxy.

Chapter 3

High-resolution simulation

From our parameter survey in Chap. 2, we now know how to perform a merger simulation favourable for distinct shell formation. With this information, we perform a high-resolution merger simulation of two colliding galaxies and their formation into a shell galaxy. We present this in the form of a self-contained paper.

MNRAS **000**, 1–11 (2022) Preprint 15 June 2022 Compiled using MNRAS LATEX style file v3.0

From starburst to quenching: merger-driven evolution of the star formation regimes in a shell galaxy

Jonathan Petersson,[1]★ Florent Renaud[1]
[1]*Lund Observatory, Department of Astronomy and Theoretical Physics, Lund University, Box 43, SE-221 00 Lund, Sweden*

Accepted XXX. Received YYY; in original form ZZZ

ABSTRACT

Recent observations of young massive star clusters in the prominent outer shell of NGC 474, raise questions about the star formation activity in shell-forming mergers and the shell galaxies that they leave behind. In this study, we perform an idealised (non-cosmological) simulation of two merging galaxies and their formation into a shell galaxy. The merger generates an excess of dense gas, and makes the star formation activity go into a starburst phase. For spatially resolved star formation, the Kennicutt-Schmidt relation varies with the merger, but with no general trend over time. Mixing between HI and H_2 produces a break in the relation at low gas surface densities, where H_2 has a better correlation to the surface density of SFR than that of all the gas, while HI has no correlation at all. Regions of star formation therefore coincide with regions of large amounts of H_2, such as the nucleus, spiral arms, and occasionally in the outskirts early in the merger. Tidal interactions during the merger scatter stars into a stellar spheroid. At coalescence, this leads to morphological quenching, and star formation stops without the need of AGN feedback. Only the innermost ∼1.5 kpc is left with star-forming H_2 gas. Since the first shells do not appear until after coalescence, shells do not host any in situ star formation. Our results suggest that shell-forming mergers can be part of the process in turning blue late-type galaxies into a red and dead early-type ones. Similarly, shell-forming mergers can also be part of the compaction model, which explains the existence of red nuggets at high redshift.

Key words: methods: numerical – galaxies: interactions – galaxies: star formation

1 INTRODUCTION

In the current cosmological paradigm, galaxy interactions and mergers are natural recurring events (White & Rees 1978), often in association with starbursts and enhanced star formation activity (Sanders & Mirabel 1996; Canalizo & Stockton 2001; Knapen et al. 2015). With the development of more powerful computers throughout the last few decades, numerical simulations have provided a theoretical framework to understand the evolution and underlying physics of the star formation activity in a wide diversity of interacting galaxies and mergers (Hernquist 1989; Barnes & Hernquist 1991; Mihos & Hernquist 1996). Idealised (non-cosmological) merger simulations have proven to be especially useful for this, because they allow to recreate specific tidally distorted galaxies (Toomre & Toomre 1972), and enable analysis of the star formation activity at a high spatial resolution (Karl et al. 2010; Teyssier et al. 2010; Renaud et al. 2014; Moreno et al. 2015; Renaud et al. 2018).

One particular class of tidally distorted galaxies are shell galaxies (Arp 1966), which are characterised by their wide concentric stellar arc(s), extending out to large galactocentric distances with sharp outer edges. Observations have shown that shells are more frequent around red early-type galaxies than blue late-type ones (Atkinson et al. 2013), and it has been estimated that ∼20% of elliptical and lenticular galaxies exhibit one or more shells (Malin & Carter 1983; Tal et al. 2009; Duc et al. 2015; Pop et al. 2018; Bílek et al. 2020) (however, see also Krajnović et al. 2011).

Several formation mechanisms have been proposed for shells over the recent decades (for a review, see e.g. Ebrova 2013). The most widely accepted one is the merger scenario. Numerical simulations have inferred that shells form via near-radial intermediate to major mergers (i.e. a mass ratio ≳1:10), where shells correspond to tidally stripped stars from accreted satellite galaxies, accumulating at the apocentres of their orbits (Quinn 1984; Hernquist & Spergel 1992; Karademir et al. 2019; Pop et al. 2018). Shells therefore share a similar origin as other tidal features, such as stellar streams and tidal tails, which tend to be produced in more circular mergers (Amorisco 2015; Hendel & Johnston 2015).

Since shells (together with other tidal features) often remain visible in the galaxies' stellar haloes long after the merger event itself (Mihos et al. 2005; Martínez-Delgado et al. 2010; Duc et al. 2015; Mancillas et al. 2019b), they can serve as a powerful tool to help reconstruct assembly histories of galaxies (Romanowsky et al. 2012; Foster et al. 2014; Longobardi et al. 2015). An example of where this has been put in action, is the shell galaxy NGC 474. Two independent teams, Alabi et al. (2020) and Fensch et al. (2020), constrain NGC 474's formation history via spectral analysis of its prominent outer shell, and show evidence that are consistent with the merger scenario (further analysis of NGC 474's formation history is done in Bílek et al. 2022). Due to the low surface brightness and poor gas content of NGC 474's outer shell (Mancillas et al. 2019a), Fensch et al. (2020) complement their spectral analysis with bright point sources that are kinematically

★ E-mail: astrojpetersson@gmail.com

associated with the outer shell, such as globular clusters and planetary nebulae (including three massive clusters from Lim et al. 2017). Full spectral fitting of four massive clusters, show that at least two massive clusters have ages < 1.5 Gyr and a relatively high metallicity, while the stellar population of the shell itself have a luminosity-weighted age of ∼3.6 Gyr. Instead, the two massive clusters match a relatively young stellar population (in both age and metallicity) in the nucleus of NGC 474, i.e. far away from the tidal debris. This shows evidence of a rather complex star formation activity, and asks questions about where and when star formation takes place in shell-forming mergers and shell galaxies.

To understand how the merger-driven star formation activity in a shell galaxy evolves with time and within the system, and what the physical conditions are for it, we perform an idealised merger simulation with a orbital configuration favourable for shell formation. The paper is organised as follows. In Section 2, we present the set-up and sub-grid models of our simulation. Section 3 includes our analysis of the global and spatially resolved star formation activity, and how it relates to the shells of the system. In Section 4, we discuss the implications of our results on the formation history of NGC 474, and on shell galaxies as a whole. Section 5 presents the conclusions of our study.

2 METHOD

We run a *N*-body + hydrodynamical simulation of two colliding disk galaxies and their formation into a shell galaxy, using the Adaptive Mesh Refinement (AMR) code RAMSES (Teyssier 2002). In the following two sections, we will briefly go through our simulation set-up and some of the sub-grid models that we use for heating and cooling of gas, star formation and feedback processes.

2.1 Simulation set-up

In RAMSES, dark matter and stars are treated as collisionless particles, whereas the fluid dynamics of the gas are computed on a grid with AMR, assuming ideal mono-atomic gas with an adiabatic index $\gamma = 5/3$. The grid follows a quasi-Lagrangian refinement strategy where a cell is adaptably refined (or de-refined) to higher (or lower) resolution, depending on the amount of baryonic mass (gas + stars) in each individual cell. In our simulation, a cell is refined if it exceeds eight times the initial gas mass resolution. A cell is also allowed to refine if it contains more than eight dark matter particles. The maximum allowed refinement level corresponds to a maximum physical resolution of ∼12 pc.

The galaxy models that we use are generated in isolation using the MAGI code (Miki & Umemura 2018), both with a dark matter halo, a central bulge, a stellar and a gaseous disc. The initial parameters are provided in Table A1. These models are rendered with a total of 2 million particles (excluding the gas which is rendered on the AMR grid). The initial total mass ratio between the two galaxies is 1:2, where the more massive galaxy is henceforth referred to as our 'main galaxy' and the less massive galaxy as a 'satellite galaxy'.

In our simulation, the main galaxy is placed at the centre of a 200 kpc cube (filled with an ambient gaseous medium with a number density of 10^{-5} cm^{-3}) and the orbital parameters of the satellite are set to give it a near radial infall trajectory towards the main galaxy (with an initial inclination angle of 10° with respect to the plane of the main galaxy). The initial separation between the two galaxies is picked large enough to allow the two galaxies to relax from the artificial initial conditions and reach a steady star formation activity before the collision, yet sufficiently short to limit the computational cost, and the premature consumption of the gas reservoirs. The full orbital parameters of the main galaxy and the satellite are given in Table A2.

2.2 Sub-grid models

Cooling of gas is metallicity-dependent and determined using tabulated values from cooling functions by Sutherland & Dopita (1993) for gas temperatures of $10^{4-8.5}$ K, and from Rosen & Bregman (1995) at lower temperatures. Heating from ultraviolet background radiation is modelled according to Haardt & Madau (1996). The initial metallicity of the gas of the main galaxy and satellite is 1 $Z_\odot$ and 0.3 $Z_\odot$ respectively.

Star formation and feedback physics follows what is presented in Agertz et al. (2013). In short, star formation occurs on individual cell level and follows the star formation law:

$$\rho_{\rm SFR} = \epsilon_{\rm ff} \frac{\rho_{\rm g}}{t_{\rm ff}} \quad \text{when} \quad \rho_{\rm g} > \rho_{\rm SF}, \tag{1}$$

where $\rho_{\rm SFR}$ is the star formation rate density, $\rho_{\rm g}$ is the gas density, $\epsilon_{\rm ff} = 0.1$ is the star formation efficiency per free-fall time, $t_{\rm ff} = \sqrt{(3\pi)/(32G\rho)}$ is the free-fall time and $\rho_{\rm SF} = 100$ cm^{-1} is the star formation threshold. Star particles are generated via a Poisson sampling process (using 10^4 $M_\odot$ star particles), where each particle is treated as a single-age stellar population with a Chabrier (2003) initial mass function (IMF). Star formation is regulated via injection of energy, momentum, mass and heavy metals into surrounding gas through stellar feedback processes, which includes core-collapse SN and SNIa, stellar winds and radiation pressure. To avoid numerical overcooling in cases where the Sedov-Taylor phase of individual SNe is unresolved, we implement the model by Kim & Ostriker (2015). The number of SNe occurring at each time step is regulated via the IMF (Chabrier 2003) and the energy injected into surrounding cells is 10^{51} erg.

3 RESULTS

Figure 1 shows the evolution of the face-on stellar surface density in our merger simulation. The first distinct stellar shell appears at $t \approx 340$ Myr, and can be seen in the top right part of the galaxy. Stellar shells continues to appear (and dissipate) for at least 1 Gyr. Another pair of distinct stellar shells can be seen at $t \approx 700$ Myr and $t \approx 1040$ Myr. In Section 3.3, we investigate whether these stellar shells have an equivalent part in the gas distribution. Besides the formation of shells, the merger also changes the overall morphology of the main galaxy, from a disk to a spheroid.

3.1 Global star formation history

In Fig. 2, we show the evolution of the SFR in our simulation, from 230 Myr before to 600 Myr after the first pericentre passage (which is sufficient to cover all epochs of star formation). Before the first pericentre passage ($t < 0$), there is a pre-interaction phase with a relatively stable SFR at around 4 $M_\odot$ yr^{-1}. This is followed by an interaction phase, where the SFR increases due to the first and second pericentre passages, with several short-lived (∼30 Myr) peaks in between. Two peaks almost coincide with the pericentre passages themselves, but with the SFR peaking a few Myr after each respective passage. After $t = 250$ Myr, the SFR rapidly decreases and goes well

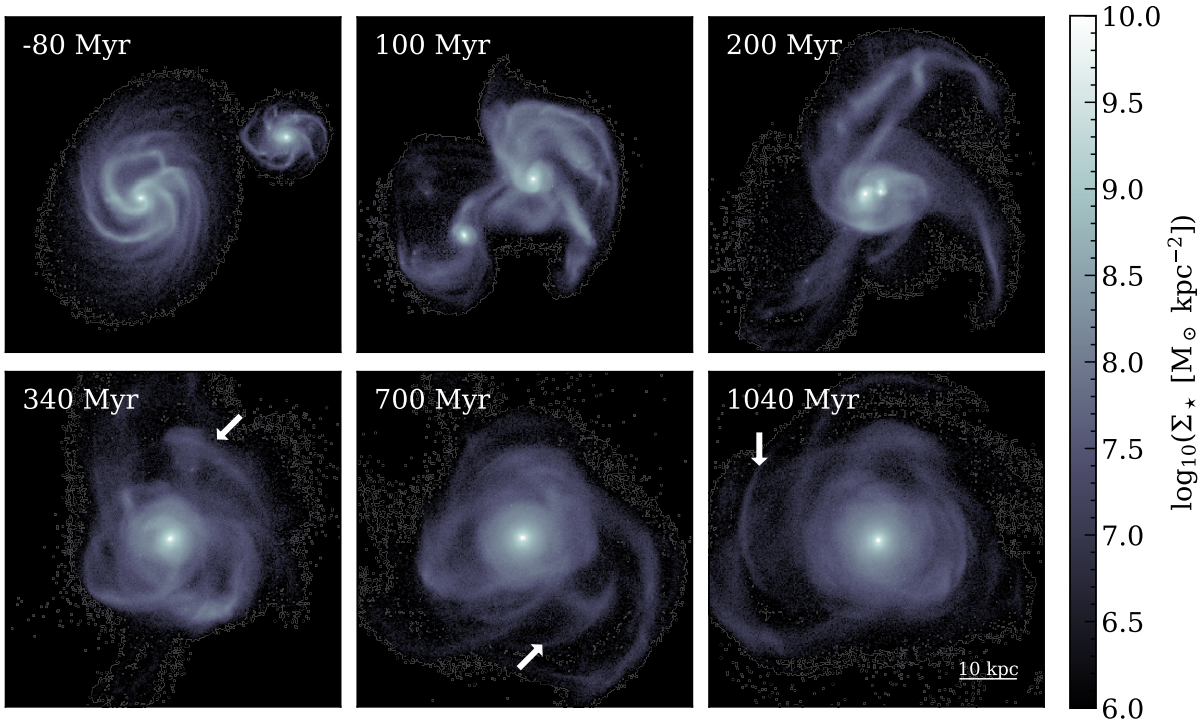

Figure 1. Face-on stellar surface density maps at six different snapshots in our simulation. We define $t = 0$ to be at the first pericentre passage. The first distinct stellar shell appears at $t = 340$ Myr and is visible in the top right part of the galaxy (see the white arrow for guidance). Another set of distinct stellar shells can be seen at $t = 700$ Myr and $t = 1040$ Myr in the bottom right and middle left part of the galaxy respectively.

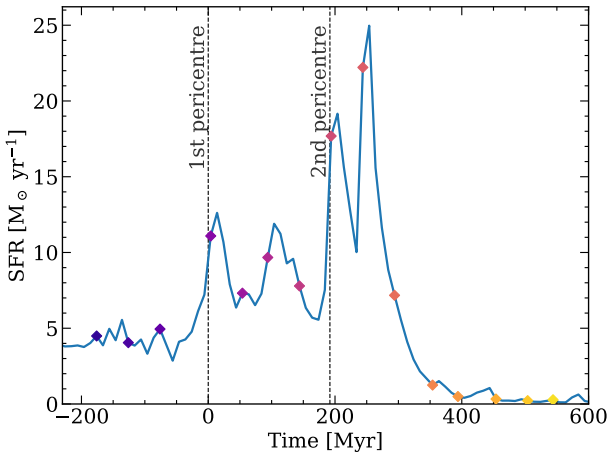

Figure 2. Evolution of the SFR in a time period sufficient to cover all epochs of star formation. The coloured symbols mark the snapshots considered in the rest of the analysis. As expected in wet mergers, the pericentre passages are associated with significant enhancements of the star formation activity.

below the initial value in the pre-interaction phase. The SFR never recovers, and this quenching phase continues throughout the rest of the simulation (i.e. for ∼4 Gyr).

To understand what physical processes are causing these distinct epochs of star formation in Fig. 2, we explore the time evolution of the SFR with respect to the gas density in a Kennicutt-Schmidt (KS) diagram. Figure 3 shows the time evolution of the surface density of gas and SFR within two times the half-mass stellar radius, initially every ∼50 Myr (as indicated in Fig. 2), and every ∼500 Myr after $t = 600$ Myr. In the pre-interaction phase, the two galaxies share similar behaviours in the KS-plane, and do not experience any drastic changes in either surface densities. For the interaction phase, the system starts with a high surface density of gas, but decreases relatively quickly while the surface density of SFR increases. This reduces the depletion time of the system (to a minimum of the order of 100 Myr), such that it goes into the starburst regime above the observed relation for (U)LIRGs (Daddi et al. 2010). The quenching phase starts with a violent decrease of the surface density of SFR, while that of the gas remains close to constant. This leads to an increase in depletion time, with a maximum reaching ∼100 Gyr.

The fact that the surface density of gas remains close to constant throughout both the starburst and quenching phase in Fig. 3, suggests that an internal redistribution of the gas density is responsible for the different phases. In Fig. 4, we show the mass-weighted probability density functions of the gas density at three different snapshots, representing the three different epochs of star formation identified in Fig. 2 and 3. For the starburst phase ($t = 200$ Myr), we see that it correlates to an excess of high density gas. Previous research has shown that several physical mechanisms can lead to an increase in mass of dense gas and/or a decrease in the depletion time, and by

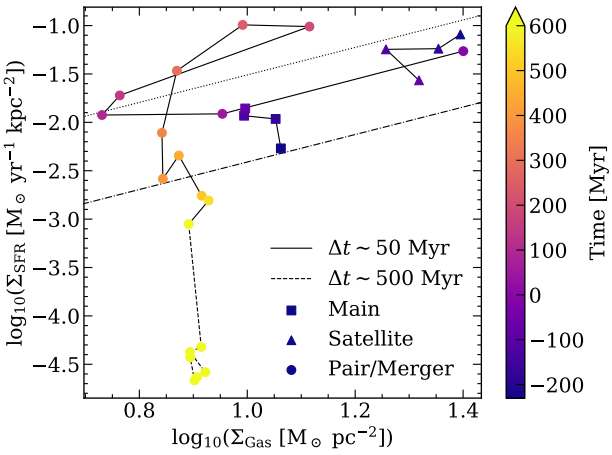

Figure 3. Time evolution of surface density of gas and SFR within two times the half-mass radius, initially every ∼50 Myr, and every ∼500 Myr after t = 600 Myr. The upper dotted line is a fit to observations of local (U)LIRGs and SMGs and the lower dash-dotted line is a fit to local spirals and z = 1.5 BzK galaxies (Daddi et al. 2010).

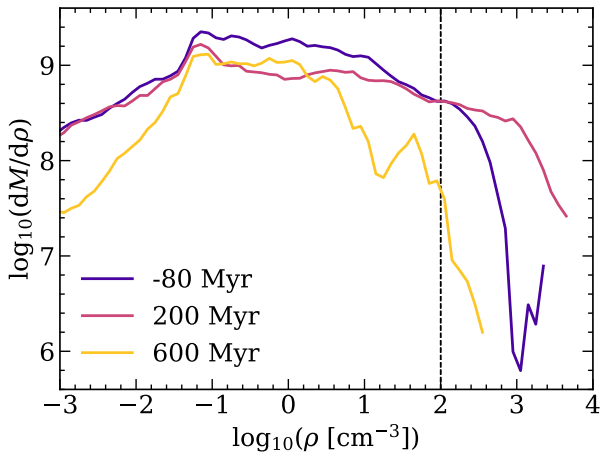

Figure 4. Mass-weighted probability distribution functions of the gas density at three snapshots, representing different epochs of star formation. This includes the pre-interaction phase (t = −80 Myr), the interaction/starburst phase (t = 200 Myr) and the quenching phase (t = 600 Myr). The dashed line marks the star formation threshold at $\rho_{\rm SF}$ = 100 cm^{-1}.

that trigger a starburst. This includes nuclear inflows induced by tidal torques (Barnes & Hernquist 1991), shocks between gas reservoirs when dense regions of the ISM overlap (Jog & Solomon 1992), and tidal and turbulent compression of gas (Renaud et al. 2014). This is further discussed in Section 4.2.

Conversely, for the quenching phase (t = 600 Myr), Fig. 4 shows a deficit of high density gas. An example of a physical process that can lead to less amounts of high density gas is the merger event itself, which can empty the gas reservoir by consuming all the gas during the starburst phase, and/or remove large amounts of the gas through tidal ejections, feedback processes and/or ram pressure stripping. However, neither Fig. 3 or 4 indicates that the gas reservoir empties.

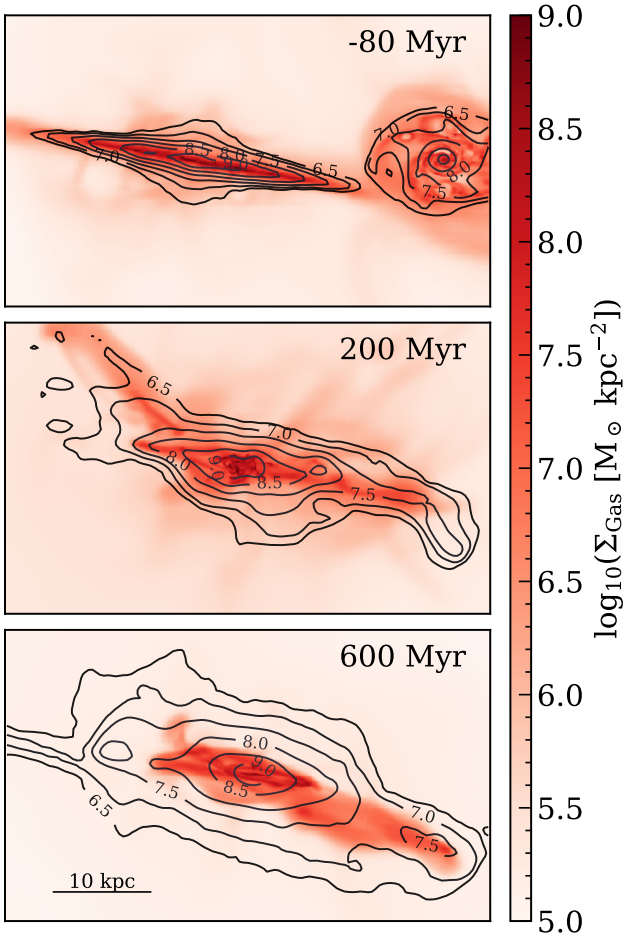

Figure 5. Edge-on surface density of gas together with contours of the stellar surface density for the same three snapshots as in Fig. 4, representing different epochs of star formation. The tidal interaction puffs up the stellar component into a spheroid, which weakens the gravitational force on the gas, and stabilises it against collapse.

During the time period −80 Myr < t < 600 Myr, the mass of gas within two times the half-mass stellar radius decreases by 2.49 × 10^9 M$_\odot$. Over the same time period, the stellar mass increases by 2.55×10^9 M$_\odot$ due to star formation. This suggests that star formation is the main contributor to the change of gas content, and that the quenching phase is not caused by a (hydro)dynamical removal of the gas reservoir.

Another example of a physical process that can lead to less amounts of high density gas is morphological quenching (Martig et al. 2009). This happens when the stellar component of a galaxy goes from a disk to a spheroid. Because of this, the gravitational potential gets shallower, and the gas disk can become stable against fragmentation and gravitational collapse, i.e. not dense enough to form stars. In Fig. 5, we illustrate the growth of a stellar spheroid in our simulation by showing the edge-on surface density of gas together with contours of the stellar surface density for the same three snapshots as in Fig. 4. The gas component also gets a more spheroidal-shape, but not to the same extent as the stellar component, probably because of its dissipative nature (see e.g. Athanassoula et al. 2016). Morphological quenching is therefore very likely the main cause for the drop in the SFR after the interaction phase.

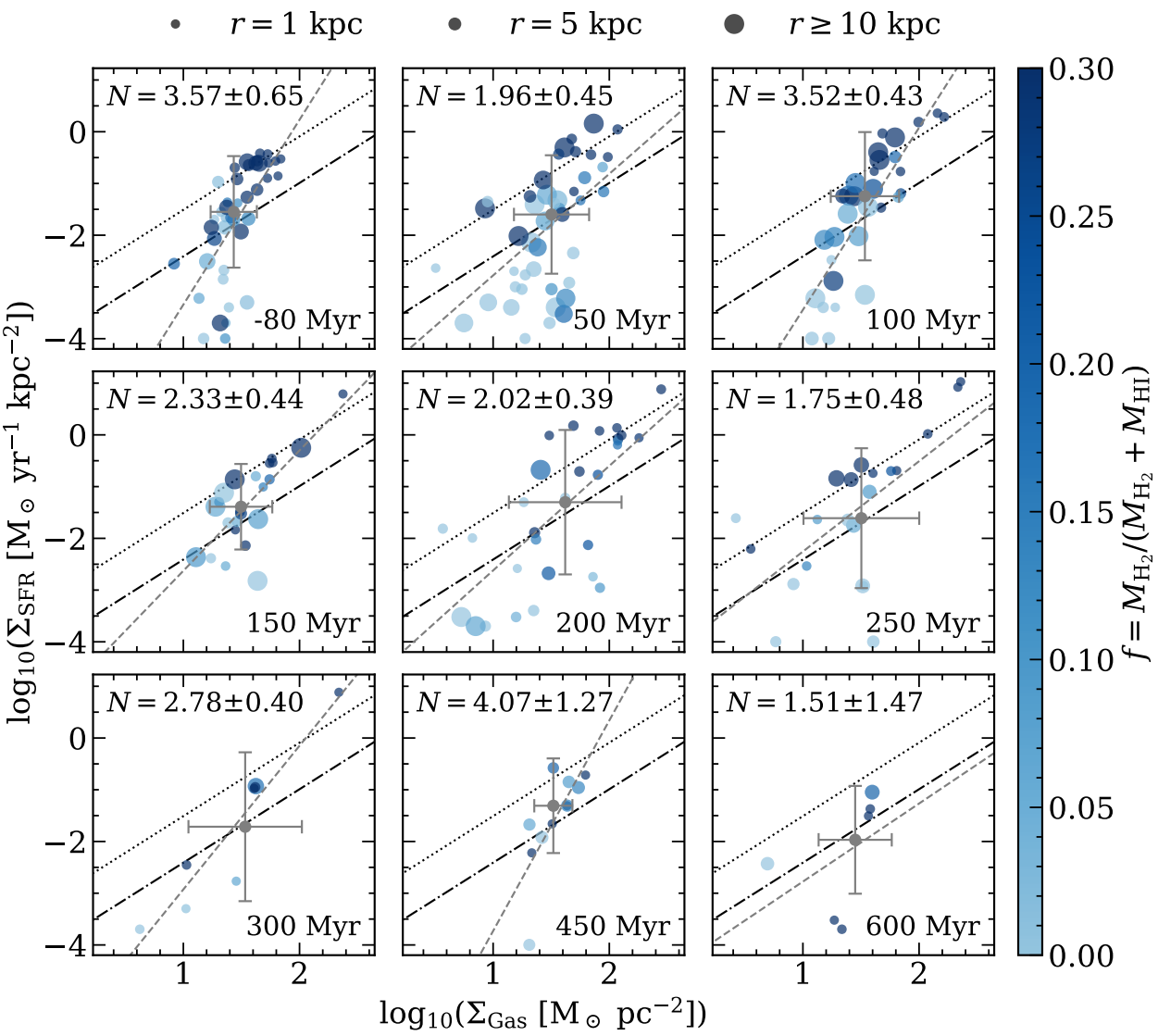

Figure 6. Spatially resolved KS-diagrams of the system at nine snapshots (chosen to include all epochs of star formation from Section 3.1) in our simulation, accounting for all the gas (i.e. molecular, atomic and ionised). Each point is a star-forming region (considering only stars younger than 10 Myr) on a 1 kpc scale, colour-coded and scaled in size according their molecular gas fraction and distance from the stellar centre of mass respectively. At $t = -80$, only star-forming regions from the main galaxy are included. For each diagram, a median value of the surface densities is calculated (grey dot), and a power-law is fitted (grey dashed line), according to the star formation law $\Sigma_{\rm SFR} \propto \Sigma_{\rm Gas}^{N}$ (Schmidt 1959; Kennicutt 1998).

3.2 Resolved star formation activity

To study the star formation activity in more detail, how it evolves within the system, and what the conditions are for it, we now focus our analysis on spatially resolved star formation. Figure 6 shows a series of KS-diagrams at nine snapshots in our simulation, where each point is a star-forming region on an 1 kpc scale, colour-coded and scaled in size according to their molecular gas fraction[1] and distance from the stellar centre of mass respectively.

For each diagram in Fig. 6, we calculate a median value of the surface densities (grey dot). The value does to seem to evolve, instead it remains within one standard deviation throughout all snapshots and show no indications of different epochs of star formation, which is a distinct different to the global case in Fig. 3.

In Fig. 6, we also fit a power-law (grey dashed line) of the form $\Sigma_{\rm SFR} \propto \Sigma_{\rm Gas}^{N}$ (Schmidt 1959; Kennicutt 1998) in each diagram. The value of the power-law index N varies strongly between snapshots, but with no general trend over time or the epoch of star formation. The uncertainty of N on the other hand, increases at late snapshots due to the quenching phase, which reduces the number of star-forming regions, making more difficult to get reliable fits. Despite the strong variation of values, N is consistently higher than the classical value of 1.4 (Schmidt 1959; Kennicutt 1998). In Fig. 6, we can also distinguish a molecular gas fraction gradient towards higher surface densities,

[1] The molecular gas fraction is defined as $f = M_{\rm H_2}/(M_{\rm H_2} + M_{\rm HI})$, where HI and H_2 are represented by cool ($T < 8000$ K, $n < 10$ cm^{-3}) and cold-dense ($T < 300$ K, $n > 10$ cm^{-3}) gas of the ISM, similarly as in Moreno et al. (2019)

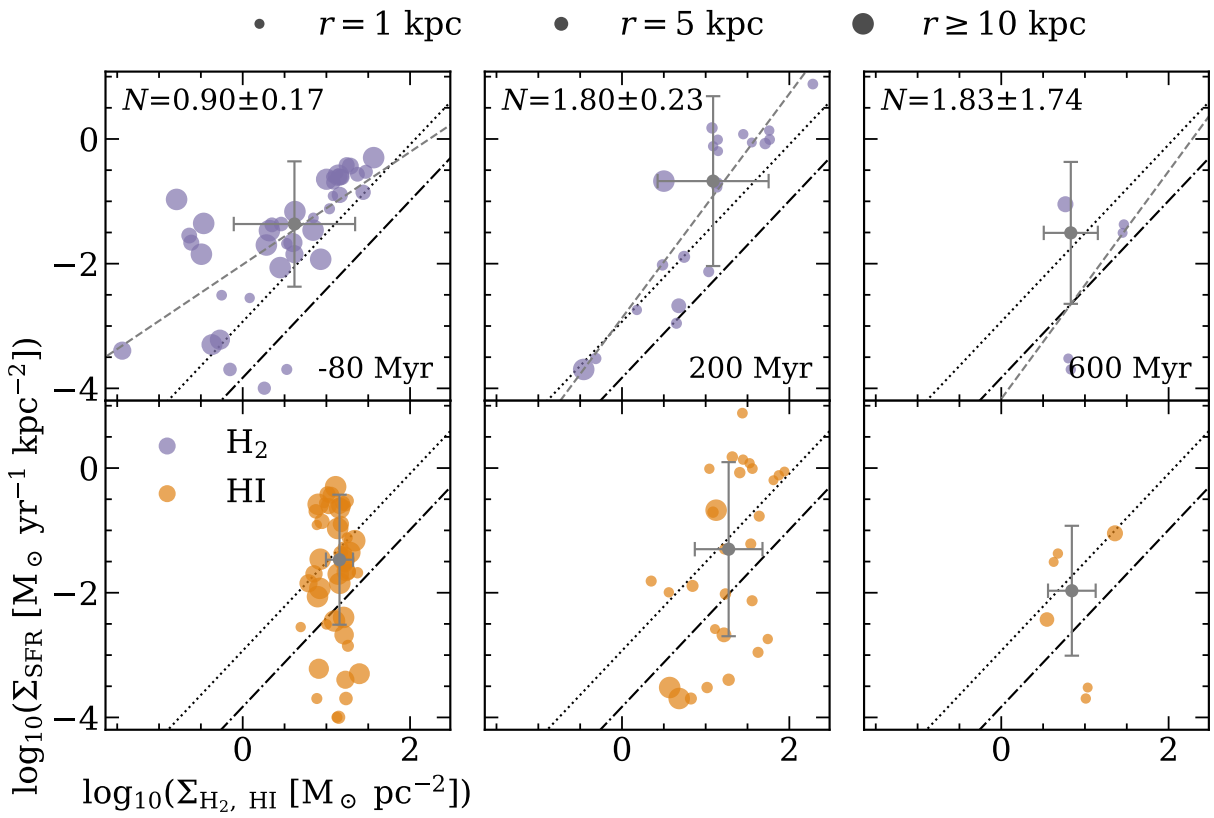

Figure 7. Similar set of KS-diagrams as in Fig. 6, but now separated into surface densities of H_2 (top) and HI (bottom), at snapshots representative for each epoch of star formation. No power-law is fitted for HI because no correlation between the surface density of SFR and HI can be distinguished.

where star-forming regions with a high molecular gas fraction have a less steep slope, better in line with that reported by observations of molecular gas only, e.g. Bigiel et al. (2008). However, contrary to Bigiel et al. (2008), there is no visible dependence of N with the galactocentric distance. We suspect that the break in the KS-distribution relates to the mixing of HI and H_2, and is responsible for the high values of N when considering all the gas.

The existence of a break in the KS-distribution at low surface densities of gas, is well known from previous research. Bigiel et al. (2008), who study the star formation law in nearby galaxies on sub-kpc scales, relates the break to the transition from an HI to an H_2-dominated ISM. However, the physical origin of the break is still debated. It has been suggested that it is not directly related to the transition from HI to H_2, but instead related to other physics that sets the ratio between the two. Krumholz et al. (2009) proposes a theoretical model in which the break and the transition from HI to H_2 is related to self-shielding of hydrogen. However, Renaud et al. (2012) with an analytical model and Kraljic et al. (2014) with the help of numerical simulations, suggest that the break is independent of self-shielding effects, and instead is linked to the transition from subsonic to supersonic turbulence in the ISM. Without going into a deeper analysis of the origin(s) of the break, which is out of scope of this paper, we point out that the break exists in all stages of the merger considered here. It is however less pronounced during the peaks of SFR, when the turbulence is expected to rise.

To explore in more detail how star-forming regions with high and low molecular gas fraction behaves differently in the KS-plane and how this produces a break in the KS-relation, we separate the total gas surface density into surface densities of HI and H_2, and examine how each relates to the surface density of SFR. In Fig. 7, three snapshots are selected for this, one for each epoch of star formation. For the surface density of H_2, we see a much better correlation with the surface density of SFR, but also a KS-relation with N close to 1, similar to the molecular KS-law found empirically in Bigiel et al. (2008). For the surface density of HI, we see the opposite effect, i.e. no correlation with the surface density of SFR, instead, HI seems to saturate at a certain surface density. In terms of depletion time, Fig. 7 shows that it is close to constant for H_2-dominated star-forming regions, while for HI, it can instead vary by several dex.

In contrast to isolated disk galaxies (Bigiel et al. 2008), no correlation between the molecular gas fraction or the depletion time with the galactocentric radius can be seen in Fig. 6 or 7. This is most likely due to the mixing induced by tidal interactions and the merger, as well as the trigger of off-centre starbursts. To investigate where star formation actually occurs (and how these regions evolve with time), we in Fig. 8 map HI and H_2 for each snapshot in Fig. 6, colour-code it according to the molecular gas fraction, and indicate star-forming regions with black contours. We can see a high molecular gas fraction in the central kiloparsecs of the two galaxies and later the merger. This is where many of the star-forming regions are located. However, we can also see star formation occurring in the spiral arms before the merger, and occasionally in the outskirts of the merger at large galactocentric distances, which very likely corresponds to areas of tidal compression (Renaud et al. 2014). As star formation slows down ($t > 250$ Myr), the off-centre star formation activity fades, and at the

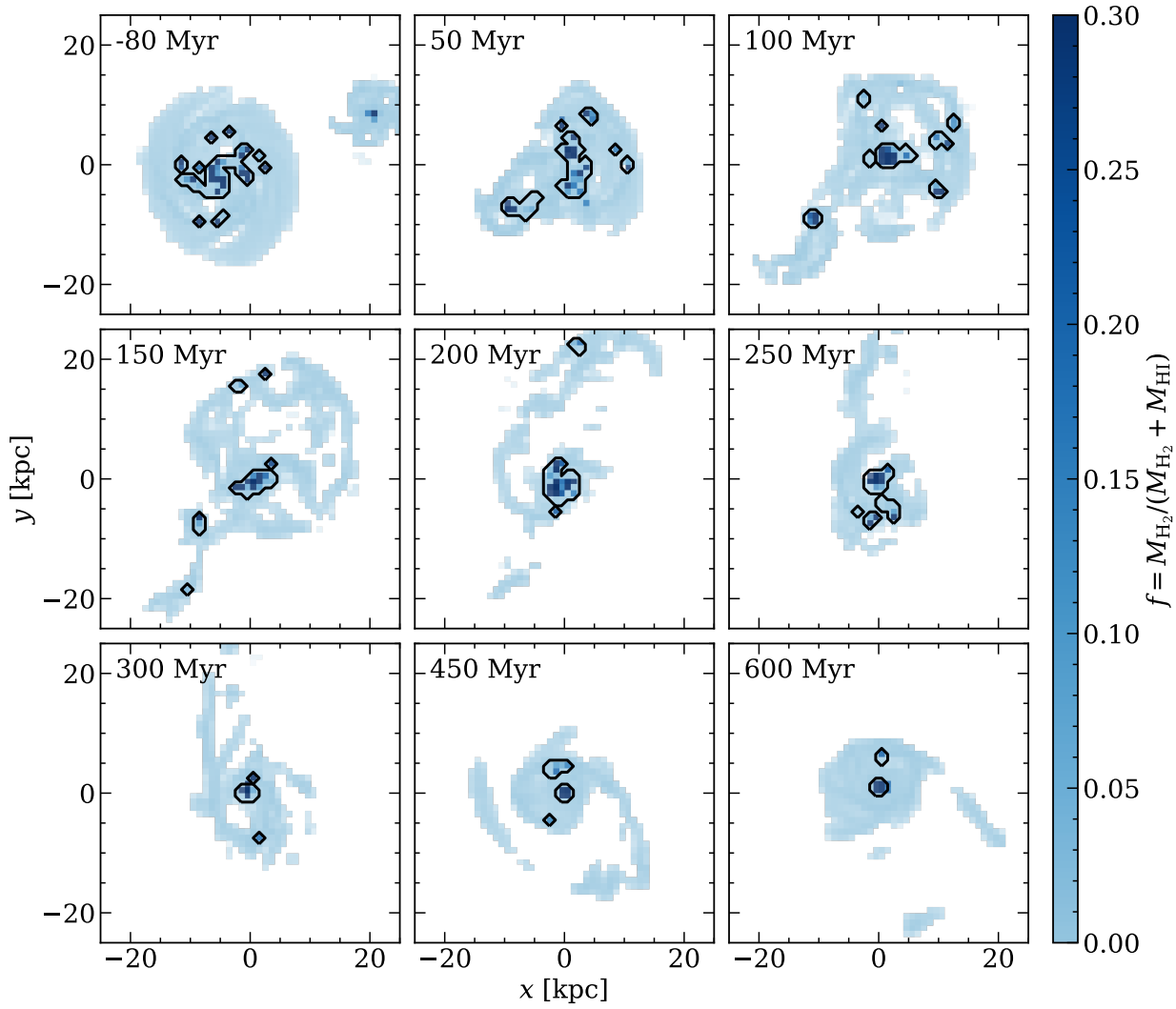

Figure 8. Face-on surface density maps of HI and H_2 for the same snapshots as in Fig. 6. The maps are colour-coded according to the molecular gas fraction at each pixel (1 kpc scale), and mass-weighted in transparency, where more opaque pixels have a higher total mass of HI and H_2 gas. The area within black contours is considered to be star-forming (contains stars younger than 10 Myr).

beginning of the quenching phase, only the innermost ~1.5 kpc is left with star-forming molecular gas.

3.3 Shells and their gas component

In Section 3.1 and 3.2, we show that when $t > 250$ Myr, the SFR drops due to morphological quenching, and that the off-centre star formation activity fades. Combined with that the first distinct stellar shells does not appear until $t > 340$ Myr, at large galactocentric distances (see Fig. 1), suggests an absence of in situ star formation in shells. In Fig. 9, we examine this in more detail by comparing the face-on surface density of gas, with contours of the stellar surface density and the location of star-forming regions (indicated with yellow stars), for the same snapshots as in Fig. 1. As expected, none of the three examples of stellar shells (bottom three panels) show evidence of in situ star formation. They all lack an equivalent shell structure in the distribution of gas as well, making them relatively gas poor, which agrees with observations of shells, e.g. the outer shell of NGC 474 (Mancillas et al. 2019a). Tidal tails on the other hand, host both in situ star formation and a gas component, e.g. in the upper part of the merger at $t = 200$ Myr. However, there are exceptions, e.g. again at $t = 200$ Myr, but now the tidal arm in the bottom right part of the merger. This difference in gas content separates shells from tidal tails, and suggests that shells can not take part in the formation of tidal dwarf galaxies (Duc & Renaud 2013).

A preliminary survey of the parameter space (not shown here), reveals that shells mainly consists of material from the disrupted satellite (Pop et al. 2018; Karademir et al. 2019). Given that the initial metallicity of the two progenitors' gas reservoirs are distinctly different, it is therefore natural to assume that the same should hold true for the gas content associated with shells, and other parts of the merger (and later the shell galaxy). In Fig. 10, we illustrate the mixing of the ISM of the two progenitors by showing gas density-weighted maps of [Fe/H] for the same snapshots as in Fig. 9, with contours of the stellar surface density and yellow stars indicating star-forming regions, similarly as in Fig. 9.

For the gas content associated with the first stellar shell at $t = 340$ Myr (top right part of the galaxy), we indeed see that it has a dis-

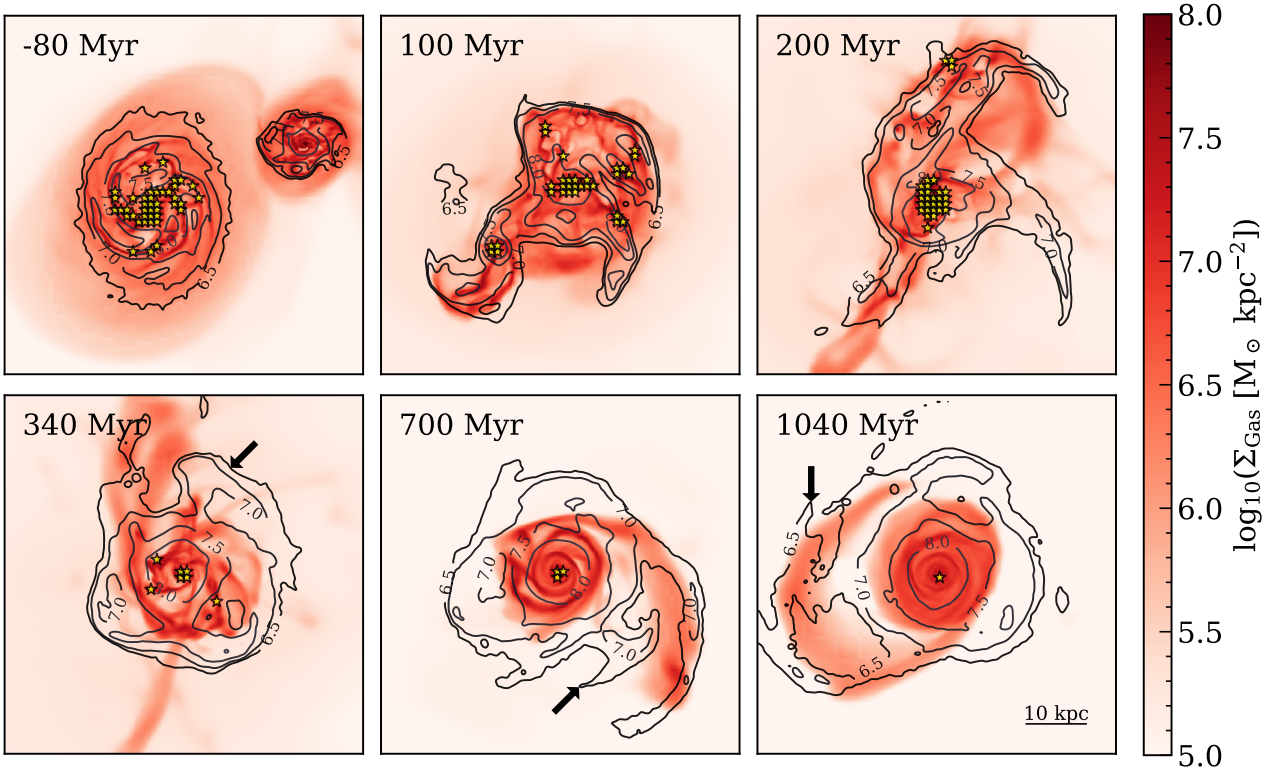

Figure 9. Face-on surface density of gas together with contours of the stellar surface density for the same six snapshots as in Fig. 1. Star-forming regions (on a 1 kpc scale) are indicated with yellow stars. Examples of stellar shells are indicated with black arrows.

tinct metallicity, yet with a non-negligible enrichment of ~0.2 dex, in comparison to the satellite's gas reservoir before first pericentre passage ($t = -80$ Myr). Within the same time period, the starburst phase enriches the ISM of the central kiloparsecs, and the maximum value of [Fe/H] increases by ~0.5 dex. However, as the ISM continues to mix, the discrepancy in metallicity between the gas content in shells and other parts of the galaxy, becomes less distinguishable, e.g. at $t = 700$ Myr in the bottom right part, and at $t = 1040$ Myr in the centre left part of the galaxy.

4 DISCUSSION

4.1 Comparison with NGC 474

Our analysis shows that a lack of molecular gas prevents in situ star formation in shells. No star formation implies no formation of star clusters, which suggests that the two young massive star clusters in the outer shell of NGC 474, identified by Fensch et al. (2020), most likely have an ex situ origin. Fensch et al. (2020) propose a formation scenario where the merger event responsible for the formation of the shells, also triggered the formation of massive star clusters via a nuclear starburst. Similarities in age and metallicity with a relatively young stellar population in the nucleus of NGC 474, indicates that this is the birth place of the young massive star clusters in the outer shell, possibly during a close passage between associated materials of the nucleus and the disrupted satellite. Despite that the limited resolution of our simulation does not allow for a detailed study on the formation of massive star clusters here, the fact that we observe a starburst phase, supports the formation scenario suggested by Fensch et al. (2020).

The argument against a formation scenario involving a nuclear starburst in NGC 474, is that its nucleus does not host any detectable remaining molecular gas (Combes et al. 2007; Mancillas et al. 2019a). The nuclear starburst must therefore have been very efficient at either consuming and/or ejecting all gas. However, this is close to the opposite of what we see in our simulation, where we still find H_2 in the central kiloparsecs after the starburst phase, and only have small amounts of (hydro)dynamical removal of gas. This difference could be due to the lack of an AGN in our simulation. An AGN fuelled by gravitational torques can efficiently remove dense molecular gas from the centre of a merger remnant, and even quench star formation (Hopkins et al. 2013). In our simulation however, quenching is reached without AGN feedback, and therefore leaves (small) amounts of molecular gas in the nucleus. We note that the two scenarios with or without an AGN could have different signatures in the molecular gas content, and can therefore serve as a tool to observationally identify the cause of quenching in these types of mergers. For NGC 474, there have been no reports (that we are aware of) showing evidence of an AGN in its nucleus. To further explore the nuclear starburst scenario, it calls complementary observations of the nucleus of NGC 474, both of its molecular gas and the presence of a AGN, or more advanced numerical simulations accounting for the possibility of igniting an AGN.

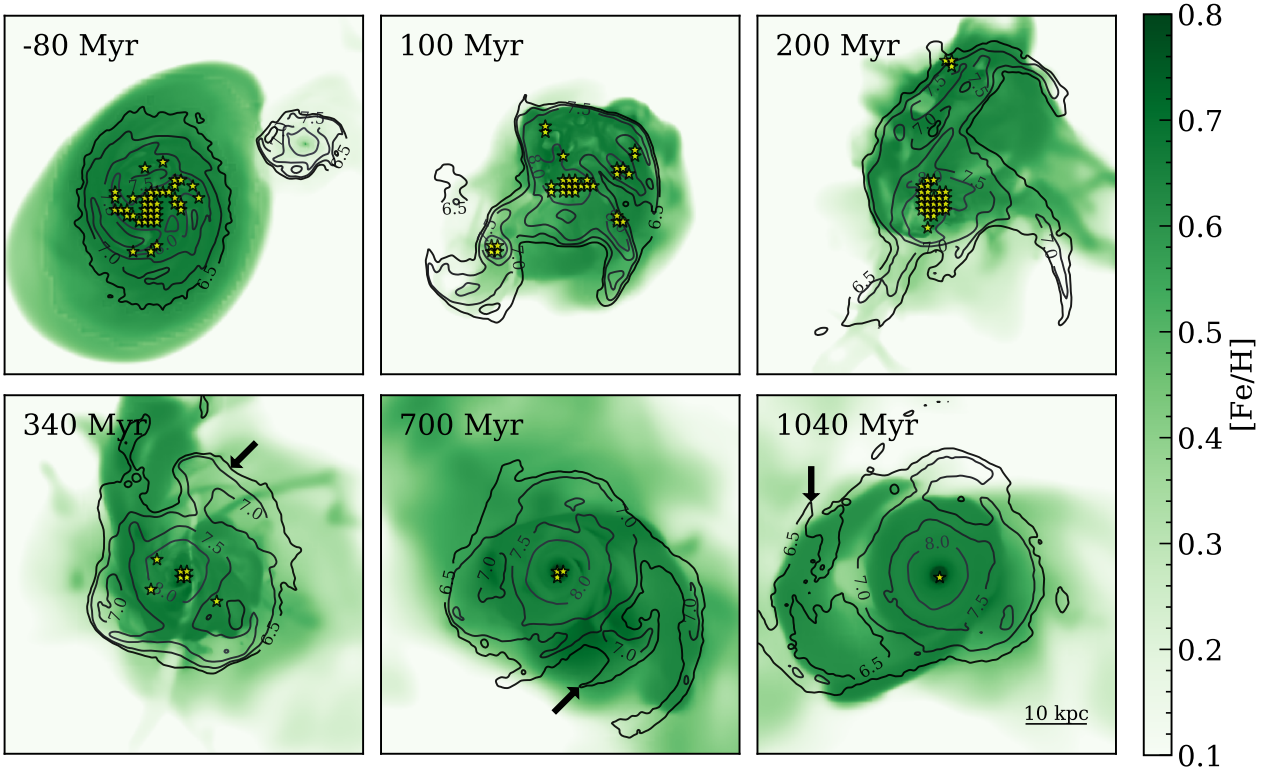

Figure 10. Face-on gas density-weighted maps of [Fe/H], for the same snapshots as in Fig. 1, together with contours of the stellar surface density and yellow stars indicating star-forming regions, similarly as in Fig. 9. Examples of stellar shells are indicated with black arrows.

4.2 Tidal compression in mergers

In Section 3.1, our analysis shows a correlation between an excess of dense gas, and the system going into the starburst regime, above the observed relation for (U)LIRGs (Daddi et al. 2010) in the KS-plane. Renaud et al. (2014, 2019) sees a similar correlation in their simulation of an Antennae-like major merger. They find that gravitational interactions between two galaxies, trigger starbursts via enhanced tidal compression over large volumes, which increases and modifies the turbulence of the ISM, such that an excess of dense gas is generated. This can explain why we see star formation at large galactocentric distances in some snapshots in Fig. 8, where tidal torques and shocks between gas reservoirs and clouds are not as effective as in the nucleus. They also find that the timescale of tidal compression to the ignition of starbursts is ~10–30 Myr, which can be the reason why the SFR peaks a few Myr after each pericentre passage in Fig. 2, and is not unique for our simulation (e.g. Moreno et al. 2019; Li et al. 2021). However, the role of tidal compression and how it relates to the excess of dense gas in our simulation, is out of scope for this paper. We note that the correlation between excess of dense gas and starbursts are the same, and therefore opens up for further analysis of compressive tides in shell-forming mergers, and its ubiquity in mergers in general (Renaud et al. 2009).

4.3 Shells and the formation of red elliptical galaxies

Tidal interactions during the merger event scatter stars into a stellar spheroid. Besides the formation of shells, what is left after the merger event is an elliptical galaxy with a diffuse gas disk and very little to none star formation due to morphological quenching (Martig et al. 2009). We know from observations that shells are more frequent around red early-type galaxies (Atkinson et al. 2013). One can therefore suspect that shell-forming mergers might be associated with the process of turning blue late-type galaxies into red and dead early-type ones in galaxy evolution. If this is a generic feature of shell galaxies, the detection of shells around a galaxy could be used to determine the cause of quenching, and possibly date it. Further investigation of this calls for more numerical simulations, which would provide valuable statistics on e.g what effects the orbital properties and mass ratio have on the quenching of the star formation activity. Numerical simulations in a cosmological context would provide valuable information on the importance of shell-forming mergers at different redshift, and how continuous accretion of gas affects the quenching phase, possibly by rejuvenating the remnant.

We note that our simulation have similarities with the compaction model by Dekel & Burkert (2014), which explains the origin of compact, quenched spheroids 'red nuggets' at high redshift. Similar to the model, our simulation also starts with a blue disk galaxy. A wet merger leads to gas contraction and forms a system with high SFR, i.e. a blue nugget. This corresponds to the starburst phase in our merger. The compactness of the blue nugget triggers an internal quenching, and turns the system into a so-called red nugget with low SFR (that can later decompactify into a spheroid). In our case, we see a drop in the SFR due to morphological quenching due to the presence of a stellar spheroid. All this together suggests that shell-forming mergers can be part of the process in turning blue nuggets into red ones at high redshift.

5 CONCLUSIONS

We perform a N-body + hydrodynamical simulation of two merging galaxies and their formation into a shell galaxy. We first analyse the star formation history on a global scale, and later the spatially resolved star formation activity, to examine how star formation evolves with time, within the system, and the conditions for it. Our main findings are as follows.

(i) As the system approaches the first pericentre passage, the star formation activity goes into a starburst phase with enhanced SFR and reduced depletion time. This is due to an excess of dense gas, likely generated by various physical processes, such as nuclear inflows, shocks, and tidal and turbulent compression.

(ii) The star formation activity later transitions into a quenching phase, where a deficit of dense gas leads to a reduced SFR and longer depletion time. We show that the main cause for this is morphological quenching, in which a stellar spheroid (formed by the scatter of stars during the merger) with its shallow gravitational potential prevents gas to collapse and get dense enough to form stars. The star formation activity never recovers and this quenching phase continues throughout the rest of the simulation.

(iii) For spatially resolved star formation on an 1 kpc-scale, the Kennicutt-Schmidt relation varies along the merger, but does not show any general trend over time. At low gas surface densities, mixing of HI and H_2 produces as break in the relation. The surface density of H_2 has a better correlation with the surface density of SFR than that of all the gas, while for HI, it is the opposite with no correlation at all, as previously found in observations of isolated disks.

(iv) Star formation takes place in regions with high molecular gas fraction. This includes the nucleus, spiral arms, and occasionally, the outskirts early in merger. At coalescence, morphological quenching stops star formation without the need of AGN feedback, and only the innermost ~1.5 kpc is left with star-forming H_2, but with a SFR 1 dex lower than before the interaction.

(v) The first stellar shells do not appear until after coalescence, and do not host any in situ star formation.

(vi) We note similarities with the compaction model by Dekel & Burkert (2014), and conclude that shell-forming mergers might be part of the process in turning blue nuggets into red ones at high redshift.

Our focus in this work is on star formation in general, and not on the formation of clusters. To further constrain the origin of the two young massive clusters in the outer shell of NGC 474, a dedicated study on the formation of massive star clusters in shell-forming mergers is needed. A simulation with an orbital configuration meant to reproduce NGC 474, would be beneficial for this type of study as well, and give a more reliable analysis.

ACKNOWLEDGEMENTS

FR acknowledges support from the Knut and Alice Wallenberg Foundation. The simulations have been performed on the Tetralith supercomputer hosted at NSC (Linköping, Sweden), thanks to a SNIC allocation.

DATA AVAILABILITY

The data underlying this article will be shared on reasonable request to the corresponding author.

REFERENCES

Agertz O., Kravtsov A. V., Leitner S. N., Gnedin N. Y., 2013, The Astrophysical Journal, 770, 25
Alabi A. B., Ferré-Mateu A., Forbes D. A., Romanowsky A. J., Brodie J. P., 2020, MNRAS, 497, 626
Amorisco N. C., 2015, MNRAS, 450, 575
Arp H., 1966, ApJS, 14, 1
Athanassoula E., Rodionov S. A., Peschken N., Lambert J. C., 2016, ApJ, 821, 90
Atkinson A. M., Abraham R. G., Ferguson A. M. N., 2013, ApJ, 765, 28
Barnes J. E., Hernquist L. E., 1991, ApJ, 370, L65
Bigiel F., Leroy A., Walter F., Brinks E., de Blok W. J. G., Madore B., Thornley M. D., 2008, AJ, 136, 2846
Bílek M., et al., 2020, MNRAS, 498, 2138
Bílek M., Fensch J., Ebrová I., Nagesh S. T., Famaey B., Duc P.-A., Kroupa P., 2022, A&A, 660, A28
Canalizo G., Stockton A., 2001, ApJ, 555, 719
Chabrier G., 2003, PASP, 115, 763
Combes F., Young L. M., Bureau M., 2007, MNRAS, 377, 1795
Daddi E., et al., 2010, ApJ, 714, L118
Dekel A., Burkert A., 2014, MNRAS, 438, 1870
Duc P.-A., Renaud F., 2013, in Souchay J., Mathis S., Tokieda T., eds, , Vol. 861, Lecture Notes in Physics, Berlin Springer Verlag. p. 327, doi:10.1007/978-3-642-32961-6_9
Duc P.-A., et al., 2015, MNRAS, 446, 120
Ebrova I., 2013, arXiv e-prints, p. arXiv:1312.1643
Fensch J., et al., 2020, A&A, 644, A164
Foster C., et al., 2014, MNRAS, 442, 3544
Haardt F., Madau P., 1996, ApJ, 461, 20
Hendel D., Johnston K. V., 2015, MNRAS, 454, 2472
Hernquist L., 1989, Nature, 340, 687
Hernquist L., Spergel D. N., 1992, ApJ, 399, L117
Hopkins P. F., Cox T. J., Hernquist L., Narayanan D., Hayward C. C., Murray N., 2013, MNRAS, 430, 1901
Jog C. J., Solomon P. M., 1992, ApJ, 387, 152
Karademir G. S., Remus R.-S., Burkert A., Dolag K., Hoffmann T. L., Moster B. P., Steinwandel U. P., Zhang J., 2019, MNRAS, 487, 318
Karl S. J., Naab T., Johansson P. H., Kotarba H., Boily C. M., Renaud F., Theis C., 2010, ApJ, 715, L88
Kennicutt Robert C. J., 1998, ApJ, 498, 541
Kim C.-G., Ostriker E. C., 2015, ApJ, 802, 99
Knapen J. H., Cisternas M., Querejeta M., 2015, MNRAS, 454, 1742
Krajnović D., et al., 2011, MNRAS, 414, 2923
Kraljic K., Renaud F., Bournaud F., Combes F., Elmegreen B., Emsellem E., Teyssier R., 2014, ApJ, 784, 112
Krumholz M. R., McKee C. F., Tumlinson J., 2009, ApJ, 699, 850
Li H., Vogelsberger M., Bryan G. L., Marinacci F., Sales L. V., Torrey P., 2021, arXiv e-prints, p. arXiv:2109.10356
Lim S., et al., 2017, ApJ, 835, 123
Longobardi A., Arnaboldi M., Gerhard O., Mihos J. C., 2015, A&A, 579, L3
Malin D. F., Carter D., 1983, ApJ, 274, 534
Mancillas B., Combes F., Duc P. A., 2019a, A&A, 630, A112
Mancillas B., Duc P.-A., Combes F., Bournaud F., Emsellem E., Martig M., Michel-Dansac L., 2019b, A&A, 632, A122
Martig M., Bournaud F., Teyssier R., Dekel A., 2009, ApJ, 707, 250
Martínez-Delgado D., et al., 2010, AJ, 140, 962
Mihos J. C., Hernquist L., 1996, ApJ, 464, 641
Mihos J. C., Harding P., Feldmeier J., Morrison H., 2005, ApJ, 631, L41
Miki Y., Umemura M., 2018, MNRAS, 475, 2269
Moreno J., Torrey P., Ellison S. L., Patton D. R., Bluck A. F. L., Bansal G., Hernquist L., 2015, MNRAS, 448, 1107
Moreno J., et al., 2019, MNRAS, 485, 1320
Pop A.-R., Pillepich A., Amorisco N. C., Hernquist L., 2018, MNRAS, 480, 1715
Quinn P. J., 1984, ApJ, 279, 596
Renaud F., Boily C. M., Naab T., Theis C., 2009, ApJ, 706, 67
Renaud F., Kraljic K., Bournaud F., 2012, ApJ, 760, L16

Table A1. Initial conditions for the main- and satellite galaxy.

	Main	Satellite
Dark matter halo (NFW)		
mass [$\times 10^{10}$ M$_\odot$]	48.0	24.0
scale length [kpc]	28.0	20.0
truncation radius [kpc]	100.0	50.0
Bulge (Hernquist)		
mass [$\times 10^{10}$ M$_\odot$]	0.5	0.5
scale radius [kpc]	0.3	0.7
truncation radius [kpc]	10.0	5.0
Stellar disc (exponential)		
mass [$\times 10^{10}$ M$_\odot$]	3.5	1.5
scale radius [kpc]	3.0	2.1
scale height [kpc]	0.5	0.21
truncation radius [kpc]	20.0	10.0
Gas disc (exponential)		
mass [$\times 10^{10}$ M$_\odot$]	0.45	0.23
scale radius [kpc]	4.0	2.8
scale height [kpc]	0.3	0.28
truncation radius [kpc]	30.0	15.0

Table A2. Initial orbital parameters for the two galaxies. The non-zero value of x for the spin axis of the main galaxy is what gives the satellite an initial inclination angle of $\sim 10°$ with respect to the plane of the main galaxy.

	Main	Satellite
(x, y, z) [kpc]	$(0, 0, 0)$	$(60, 20, 0)$
(v_x, v_y, v_z) [km s^{-1}]	$(0, 0, 0)$	$(-30, 0, 0)$
Spin axis (x, y, z)	$(0.1763, 0, 1)$	$(0, 0.5, 0.5)$

Renaud F., Bournaud F., Kraljic K., Duc P. A., 2014, MNRAS, 442, L33
Renaud F., et al., 2018, MNRAS, 473, 585
Renaud F., Bournaud F., Agertz O., Kraljic K., Schinnerer E., Bolatto A., Daddi E., Hughes A., 2019, A&A, 625, A65
Romanowsky A. J., Strader J., Brodie J. P., Mihos J. C., Spitler L. R., Forbes D. A., Foster C., Arnold J. A., 2012, ApJ, 748, 29
Rosen A., Bregman J. N., 1995, ApJ, 440, 634
Sanders D. B., Mirabel I. F., 1996, ARA&A, 34, 749
Schmidt M., 1959, ApJ, 129, 243
Sutherland R. S., Dopita M. A., 1993, ApJS, 88, 253
Tal T., van Dokkum P. G., Nelan J., Bezanson R., 2009, AJ, 138, 1417
Teyssier R., 2002, A&A, 385, 337
Teyssier R., Chapon D., Bournaud F., 2010, ApJ, 720, L149
Toomre A., Toomre J., 1972, ApJ, 178, 623
White S. D. M., Rees M. J., 1978, MNRAS, 183, 341

APPENDIX A: INITIAL CONDITIONS

This paper has been typeset from a TEX/LATEX file prepared by the author.

Chapter 4

Conclusions

In conclusion, with a parameter survey of low-resolution merger simulations, we find a set initial conditions favourable for shell formation. With these initial conditions, we perform a high-resolution simulation of a shell-forming merger and its formation into a shell galaxy, and present it in the form of a self-contained paper in Chap. 3. However, our parameter survey is relatively short with 11 simulations, which brings limitations on much depth we can analyse each different parameter. Because of these limitations, there are therefore potentially other sets of initial conditions, just as, or even more favourable for shell formation. Further investigation of this calls for a more extensive parameter survey, in which we can study the influence of a specific parameter on shell formation in more detail, and explore other parameters. In our survey, we limit ourselves to four different parameters (or properties): mass ratio, pericentre distance, inclination angle (with respect to the plane of the main galaxy) and the morphology of the satellite. The reason why we select these specific parameters is because they have proven to be especially important in previous research on the formation mechanisms of shells (e.g. Pop et al., 2018). However, this does not exclude the possibility of other parameters also having an important impact on shell formation (e.g. the velocity of the satellite at impact).

With a more extensive parameter survey, improvements can be made on the detection of shells. In this work, we detect shells via overdensities in the stellar surface density profiles, together with a visual inspection of the stellar surface density map of the system. This makes the method somewhat subjective, and not ideal for a larger sample of simulations. Quantifying shells in terms of their stellar surface density, allows for a more fair comparison between simulations. Comparison of shells within a consistent narrow time frame from the first pericentre passage, would also give a more reliable analyses (which was somewhat difficult to obtain in our survey due to limitations in number of snapshots with raw data). The connection between shells and their wrap in phase-space (which we illustrate in Fig. 1.3 and 1.4), can potentially serve as an additional detection method for shells. However, to develop or use such a technique, it requires more analysis and study of the physics behind the phase-space wrapping model by Quinn (1984).

On a final note, we want to discuss the implications of our results on the possibility of shells around the Milky Way. Assuming that our results from Chap. 3 is applicable to all shell-forming mergers, it suggests that the presence of shells is directly correlated to quenched star formation of a system. The Milky Way however, is still star-forming (for a review, see e.g. Kennicutt & Evans, 2012), which from our assumption means that the Galaxy does not host any shells, and i.e. therefore contradicts previous indications of shells around the Milky Way (Deason et al., 2013; Donlon et al., 2020). However, this is only valid in an idealised context, and therefore calls for more complex simulations in a cosmological context, where continues accretion of gas can potentially restart star formation by rejuvenating the Galaxy.

Bibliography

Amorisco N. C., 2015, MNRAS, 450, 575

Arnaboldi M., Ventimiglia G., Iodice E., Gerhard O., Coccato L., 2012, A&A, 545, A37

Arp H., 1966, ApJS, 14, 1

Atkinson A. M., Abraham R. G., Ferguson A. M. N., 2013, ApJ, 765, 28

Bílek M., et al., 2020, MNRAS, 498, 2138

Canalizo G., Bennert N., Jungwiert B., Stockton A., Schweizer F., Lacy M., Peng C., 2007, ApJ, 669, 801

Charmandaris V., Combes F., van der Hulst J. M., 2000, A&A, 356, L1

Deason A. J., Van der Marel R. P., Guhathakurta P., Sohn S. T., Brown T. M., 2013, ApJ, 766, 24

Donlon Thomas I., Newberg H. J., Sanderson R., Widrow L. M., 2020, ApJ, 902, 119

Duc P.-A., et al., 2011, MNRAS, 417, 863

Duc P.-A., et al., 2015, MNRAS, 446, 120

Dupraz C., Combes F., 1986, A&A, 166, 53

Ebrová I., Jílková L., Jungwiert B., Křížek M., Bílek M., Bartošková K., Skalická T., Stoklasová I., 2012, A&A, 545, A33

Fensch J., et al., 2020, A&A, 644, A164

Fort B. P., Prieur J. L., Carter D., Meatheringham S. J., Vigroux L., 1986, ApJ, 306, 110

Foster C., et al., 2014, MNRAS, 442, 3544

Freeman K. C., 1970, ApJ, 160, 811

Hendel D., Johnston K. V., 2015, MNRAS, 454, 2472

Hernquist L., Spergel D. N., 1992, ApJ, 399, L117

Johnston K. V., Bullock J. S., Sharma S., Font A., Robertson B. E., Leitner S. N., 2008, ApJ, 689, 936

Karademir G. S., Remus R.-S., Burkert A., Dolag K., Hoffmann T. L., Moster B. P., Steinwandel U. P., Zhang J., 2019, MNRAS, 487, 318

Kennicutt R. C., Evans N. J., 2012, ARA&A, 50, 531

Longobardi A., Arnaboldi M., Gerhard O., Mihos J. C., 2015, A&A, 579, L3

Malin D. F., Carter D., 1983, ApJ, 274, 534

Mancillas B., Combes F., Duc P. A., 2019a, A&A, 630, A112

Mancillas B., Duc P.-A., Combes F., Bournaud F., Emsellem E., Martig M., Michel-Dansac L., 2019b, A&A, 632, A122

Martínez-Delgado D., et al., 2010, AJ, 140, 962

Merrifield M. R., Kuijken K., 1998, MNRAS, 297, 1292

Mihos J. C., Harding P., Feldmeier J., Morrison H., 2005, ApJ, 631, L41

Miki Y., Umemura M., 2018, MNRAS, 475, 2269

Pop A.-R., Pillepich A., Amorisco N. C., Hernquist L., 2018, MNRAS, 480, 1715

Quinn P. J., 1984, ApJ, 279, 596

Romanowsky A. J., Strader J., Brodie J. P., Mihos J. C., Spitler L. R., Forbes D. A., Foster C., Arnold J. A., 2012, ApJ, 748, 29

Tal T., van Dokkum P. G., Nelan J., Bezanson R., 2009, AJ, 138, 1417

Teyssier R., 2002, A&A, 385, 337

Thronson Harley A. J., Bally J., Hacking P., 1989, AJ, 97, 363

Turnbull A. J., Bridges T. J., Carter D., 1999, MNRAS, 307, 967

Weil M. L., Hernquist L., 1993, ApJ, 405, 142

White S. D. M., Rees M. J., 1978, MNRAS, 183, 341

Appendix A

Additional plots

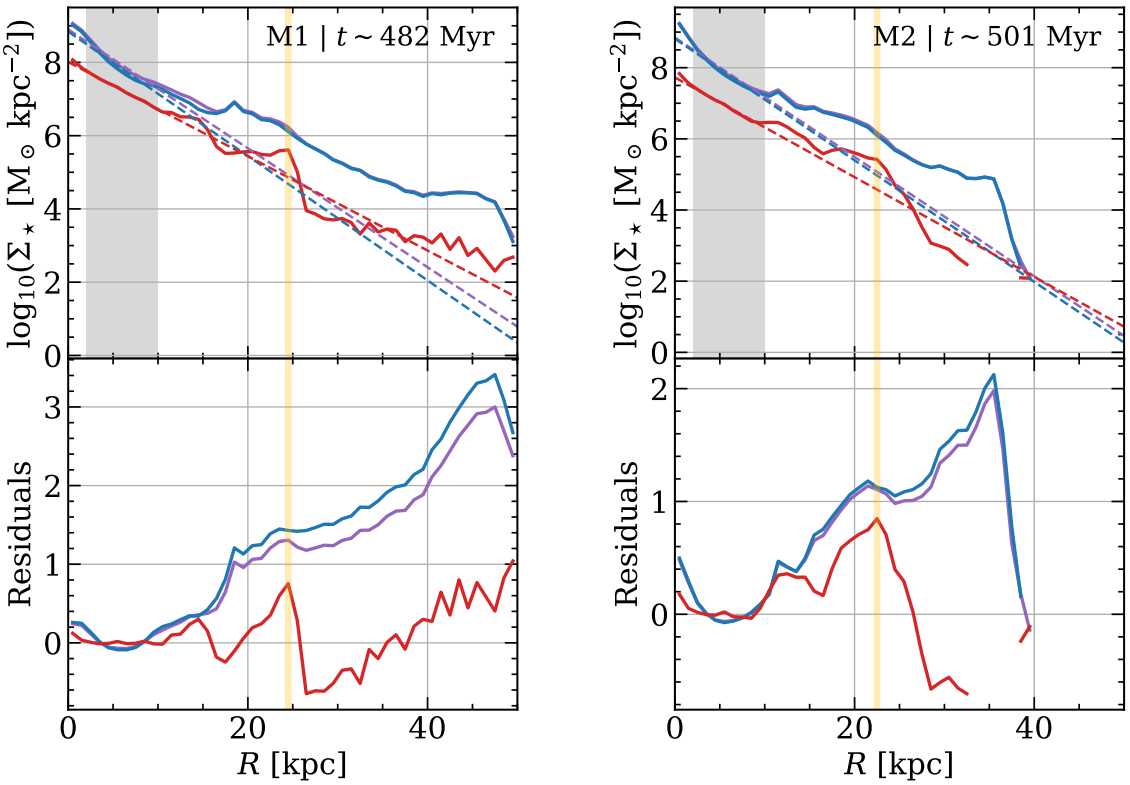

Figure A.1: Stellar surface density profiles, one for each galaxy and one with both galaxies combined, and residual plots made from subtracting each stellar surface density profile with their respective exponential fit (dashed lines, fitted from data inside the grey area), for all simulations (except the fiducial rune) in our parameter survey (see Table 2.1 in Chap. 2). Yellow lines marks relatively sharp peaks in the residuals plots and therefore potential shells.

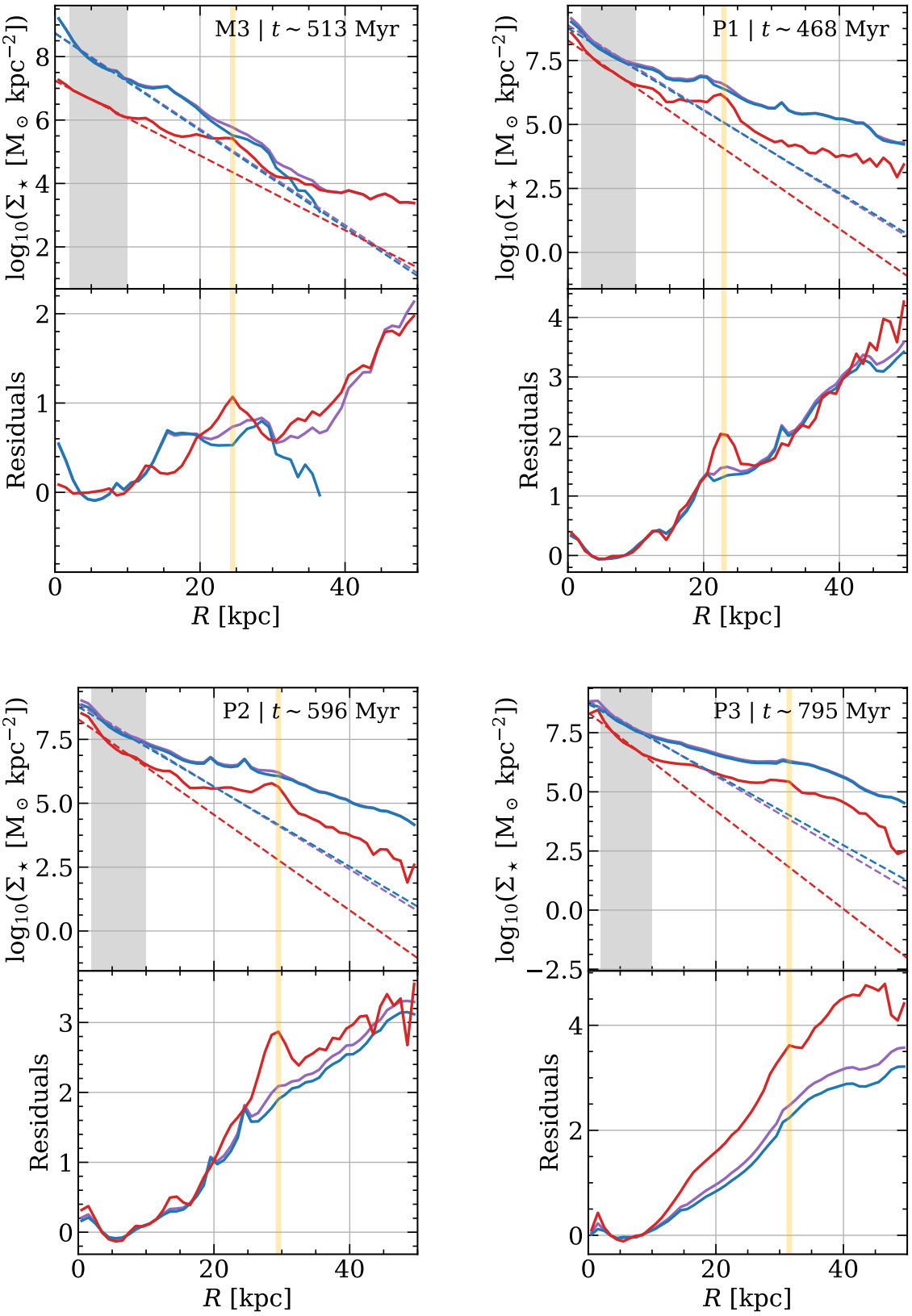

Figure A.2: Continuation of Fig. A.1

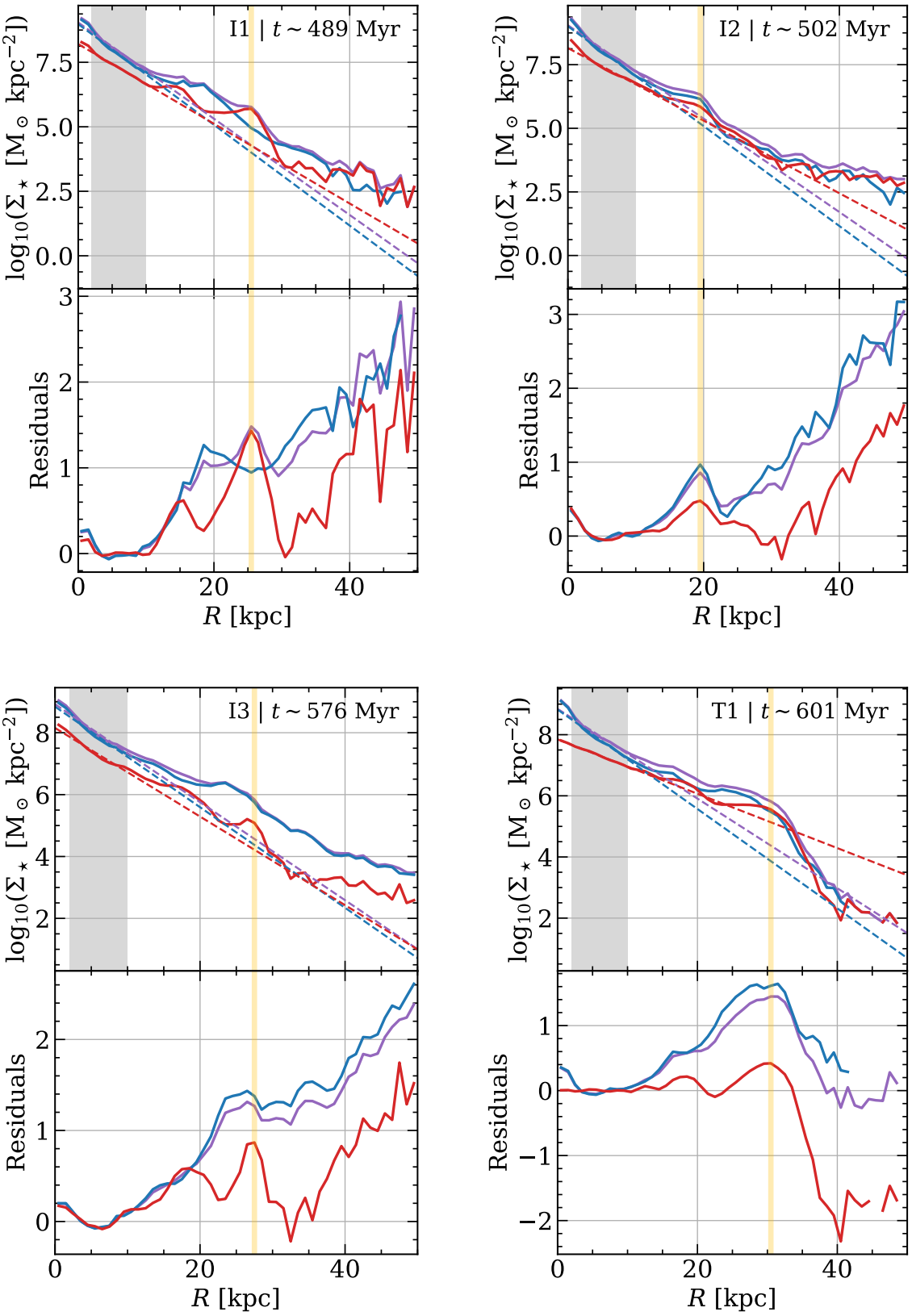

Figure A.3: Continuation of Fig. A.1

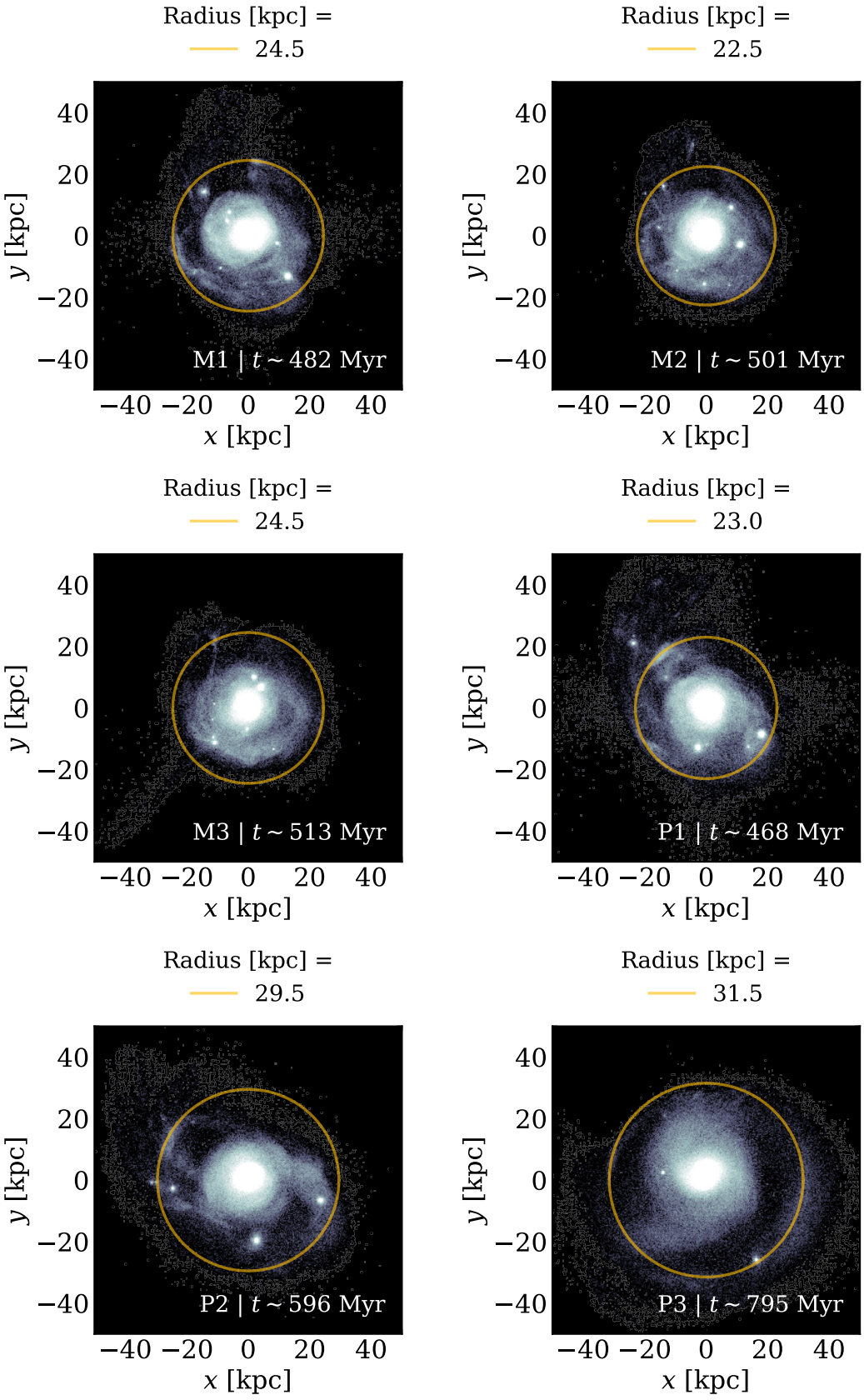

Figure A.4: Stellar surface density maps for all simulations (except the fiducial run) in our parameter survey (see Table 2.1 in Chap. 2. Yellow circles corresponds to yellow vertical lines in each simulations respective plot in Fig. A.1–A.3.

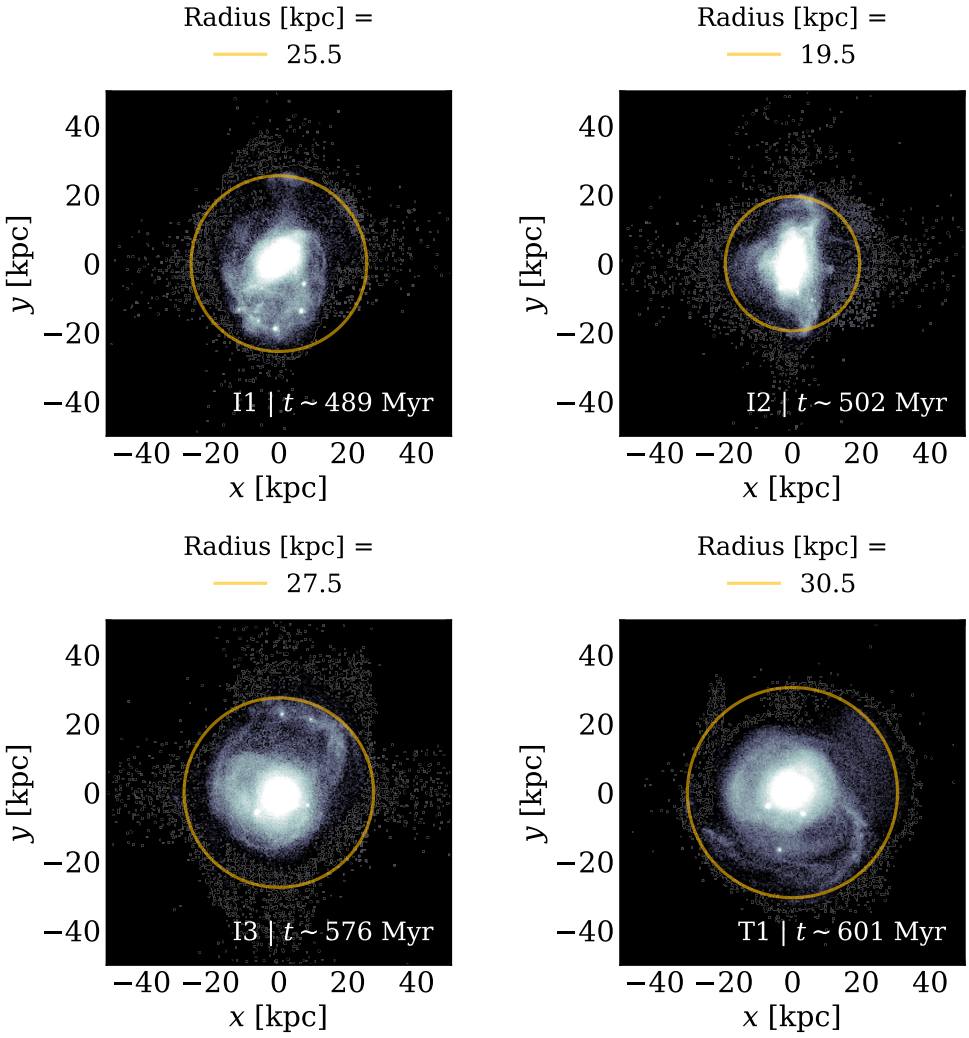

Figure A.5: Continuation of Fig. A.4.